Bubbles and bubbly flows

Garbin, Valeria; Bothe, Dieter; Brenn, Günter; Casciola, Carlo Massimo; Colin, Catherine; Marengo, Marco; Risso, Frédéric; Tryggvason, Gretar; Lohse, Detlef

DOI
10.1016/j.ijmultiphaseflow.2025.105240

Publication date
2025

Document Version
Final published version

Published in
International Journal of Multiphase Flow

Citation (APA)
Garbin, V., Bothe, D., Brenn, G., Casciola, C. M., Colin, C., Marengo, M., Risso, F., Tryggvason, G., & Lohse, D. (2025). Bubbles and bubbly flows. *International Journal of Multiphase Flow*, *190*, Article 105240. https://doi.org/10.1016/j.ijmultiphaseflow.2025.105240

International Journal of Multiphase Flow 190 (2025) 105240

Contents lists available at ScienceDirect

International Journal of Multiphase Flow

journal homepage: www.elsevier.com/locate/ijmulflow

50th Anniversary of IJMF

Bubbles and bubbly flows

Valeria Garbin [a,*], Dieter Bothe [b], Günter Brenn [c], Carlo Massimo Casciola [d], Catherine Colin [e], Marco Marengo [f], Frédéric Risso [e], Gretar Tryggvason [g], Detlef Lohse [h,i,*]

[a] Department of Chemical Engineering, Delft University of Technology, van der Maasweg 9, Delft, 2629 HZ, The Netherlands
[b] Institute of Mathematical Modelling and Analysis, Darmstadt University of Technology, Alarich-Weiss-Straße 10, Darmstadt, 64287, Germany
[c] Institute of Fluid Mechanics and Heat Transfer, Graz University of Technology, Inffeldgasse 25/F, Graz, 8010, Austria
[d] Department of Mechanical and Aerospace Engineering, La Sapienza University of Rome, via Eudossiana 18, Roma, 00184, Italy
[e] Institut de Mécanique des Fluides de Toulouse, Université de Toulouse, CNRS, INPT, 2 allée Camille Soula, Toulouse, 31400, France
[f] Department of Civil Engineering and Architecture, University of Pavia, via Ferrata 3, Pavia, 27100, Italy
[g] Department of Mechanical Engineering, Johns Hopkins University, 3400 North Charles Street, Baltimore, MD 21218, USA
[h] Physics of Fluids Department, Faculty of Science and Technology and J.M. Burgers Center for Fluid Dynamics, University of Twente, P.O. Box 217, Enschede, 7500 AE, The Netherlands
[i] Max–Planck Institute for Dynamics and Self-Organization, Am Fassberg 17, Goettingen, 37077, Germany

ARTICLE INFO

Keywords:
Bubbles
Bubbly flows
Bubble nucleation
Bubble dynamics
Cavitation
Mass transfer in bubbly flows

ABSTRACT

Bubbles and bubbly flows are omnipresent in nature and technology, showing a multitude of phenomena, which can be either beneficial or a hindrance. In any case, for their control and their applications, it is crucial to understand their fundamentals and therefore from the very beginning of the International Journal of Multiphase Flow they have been central. In this synoptic review we give some examples for the fascinating fluid dynamics of bubbles and bubbly flows, starting from their nucleation and cavitation phenomena, then going to single bubble phenomena, and finally to bubbly flows, in which the collective effects of bubbles are key, and to mass transfer in such bubbly flows. The review ends with an outlook on future direction and open issues in the research on bubbles and bubbly flows.

1. Introduction

In the report "Flow to the Future – Fluid Dynamics in the Netherlands" (Lohse et al., 2023), the crucial role of fluid dynamics in today's industry and for solving the societal challenges of tomorrow have been outlined, identifying fluid dynamics as a key enabling technology to protect our future. A similar report written before for the UK situation (Juniper et al., 2021) also reaches a similar conclusion, and so does the ESA White Paper (Col et al., 2021). In the Dutch report, six major societal challenges have been identified in which fluid dynamics will be a vital part of understanding and providing solutions: (i) Climate change, (ii) Environment, (iii) Energy transition and energy security, (iv) High-tech manufacturing, (v) Healthcare, and (vi) Agriculture and food production. For each of these six fields, not only fluid dynamics in general, but *bubbles and bubbly flows* in particular will be vital for understanding the challenges and for providing the solutions. Here are some examples: (i) For climate change and global warming, bubbles play a key role: they form when waves break and are a crucial vehicle for the transfer of CO_2 from the atmosphere to the ocean (Deike, 2022). Vice versa, when they rise, they finally form air pockets at the water–air interface, which eventually burst, releasing aerosols into the atmosphere (Lhuissier and Villermaux, 2012; Lohse and Villermaux, 2020; Villermaux et al., 2022; Jiang et al., 2024). (ii) For the environment, the purification of wastewater is obviously of key importance, and one of the prime techniques here is flotation (Peleka et al., 2018), where bubbles rise and attach to floating particles, taking them along, thus purifying the water. (iii) For the energy transition, a key technology is hydrogen production by electrolysis, employing renewable energies (Ardo et al., 2018; Chatenet et al., 2022). Here, emerging hydrogen bubbles can partially block the electrode, leading to a considerable reduction in the efficiency, and ways must be found to release them from the electrode at an early stage (Park et al., 2023). (iv) In high-tech manufacturing, pieozoacoustic ink-jet printing is one of the key technologies. Here, for too strong driving or too high jetting frequencies, bubbles can be entrained at the meniscus into the ink channel. These bubbles can grow by rectified diffusion, and decrement or totally hinder the droplet jetting process (Lohse, 2022).

* Corresponding authors.
E-mail addresses: v.garbin@tudelft.nl (V. Garbin), d.lohse@utwente.nl (D. Lohse).

https://doi.org/10.1016/j.ijmultiphaseflow.2025.105240
Received 25 February 2025; Accepted 31 March 2025
Available online 29 April 2025

Another example is immersion lithography, where a film of water (with a refractive index of 1.33, rather than 1.00 for air) between the wafer and the optical lens is employed, to allow for smaller structures. The bottleneck in making this technique faster is the entrainment of bubbles emerging from a contact line instability into the water, which obviously is detrimental for patterns to be created on the wafer (Bouwhuis et al., 2012). In fact, the price for which these stepper machines can be sold is set by the maximal velocity without bubble entrainment, i.e., by the hydrodynamic contact line instability. Another example in high-tech manufacturing is thermal management, where new advanced systems to cope with extremely high heat fluxes of electronic components, like for example, pulsating heat pipes, are based on the physics of bubble generation and transport (Taylor bubbles) (Nikolayev, 2021). (v) For healthcare, ultrasound diagnostics has become a highly advanced technique with fine resolution and strong signals, thanks to contrast agents, which are coated bubbles driven by ultrasound close to their resonance frequency (typically around 3 MHz) and which considerably enhance the scattering cross section of the diagnostic ultrasound (Dollet et al., 2019). Understanding the dynamics of these oscillating coated bubbles is key for further optimization of this method. (vi) Finally, for food production, we give the profane example of champagne, where bubbles are key in determining the taste and sensory experience of the drinking (Liger-Belair, 2005; Mathijssen et al., 2023) and for agriculture, we mention the sap flow within plants, which can be hindered by nucleated bubbles (Jensen et al., 2016). Some of these examples and many others were further elaborated in the recent review article "Bubble puzzle: From fundamental to applications" by one of us (Lohse, 2018).

Bubbles can exist across a wide range of length scales, from the sub-nanometer scale at nucleation, to the micrometer scale as seen in ultrasound contrast-enhancing bubbles, to the millimeter scale, such as those formed by gas injections into water via a needle or from air entrainment in the ocean. They can also reach the meter scale in acoustic marine geophysical surveys ("airgun", see for example (Giles, 1968; Li et al., 2020)) and even tens of meters in size, following underwater explosions.

Various material properties and parameters characterizing the processing are relevant for their behavior. Their combinations lead to the relevant dimensionless numbers characterizing the bubbles and their dynamics. The most relevant ones may be the Weber number, comparing inertia and capillarity, the Froude number, comparing inertia and buoyancy, the Archimedes number comparing buoyancy and viscous forces, the capillary number comparing viscous and capillary forces, and the Bond number as ratio of buoyancy and capillarity. A more complete list can be found in Lohse (2018); obviously, not all of them are independent.

Bubbles can moreover experience various types of dynamical behaviors. Depending on the situation, the dynamics of the volume can be of relevance i.e., for small enough bubbles that of its radius, or for larger ones the one of its shape, and of course of its position or relative positions. The forces which can play a role are buoyancy, inertia, acoustic forces, Marangoni forces, and viscous forces (as reflected by above given dimensionless numbers), and the bubble can exchange mass and heat with its environment. Bubbles can moreover be gaseous or consist of vapor (Prosperetti, 2017), or, more generally and commonly, contain both gases and vapor.

In 1848, at the Royal Institute in London, Michael Faraday gave a series of six lectures on the "Chemical history of a candle", as part of the "Christmas lectures for young people", teaching the audience various physical and chemical aspects of flames (Faraday, 2005). In a sense, a lecture series in the same spirit could be given on bubbles, which teach us on a plethora of physical and chemical phenomena.

Obviously, this article cannot discuss all of the rich aspects and bubble features mentioned so far. It cannot be a complete review on bubbles, even not of sub-aspects of bubbles; we can at most point the reader to good reviews on such sub-aspects and we will do so. But the article can share our fascination for bubbles with the reader and give the reader some taste of bubble problems and act as appetizer to deeper dive into the subject.

The article will proceed from small scales at which bubbles nucleate and where cavitation phenomena occur, to micro- and millimeter bubbles, and finally to collective phenomena of bubbles, including mass transfer in bubbly flows. Sketches of the various phenomena are shown in Fig. 1, where we place them in the parameter space "length scale" (x-axis) vs "number of bubbles" (y-axis). The article will end with a section on future perspectives, in which we will also point to important open ends in our understanding of bubbles and bubbly flows.

Given the nature of this article and our different main expertise, one or two of us took the lead for certain (sub)sections. For transparency, we name them at the end of the corresponding (sub)section. To start with, the lead for Section 1 was taken by D.L..

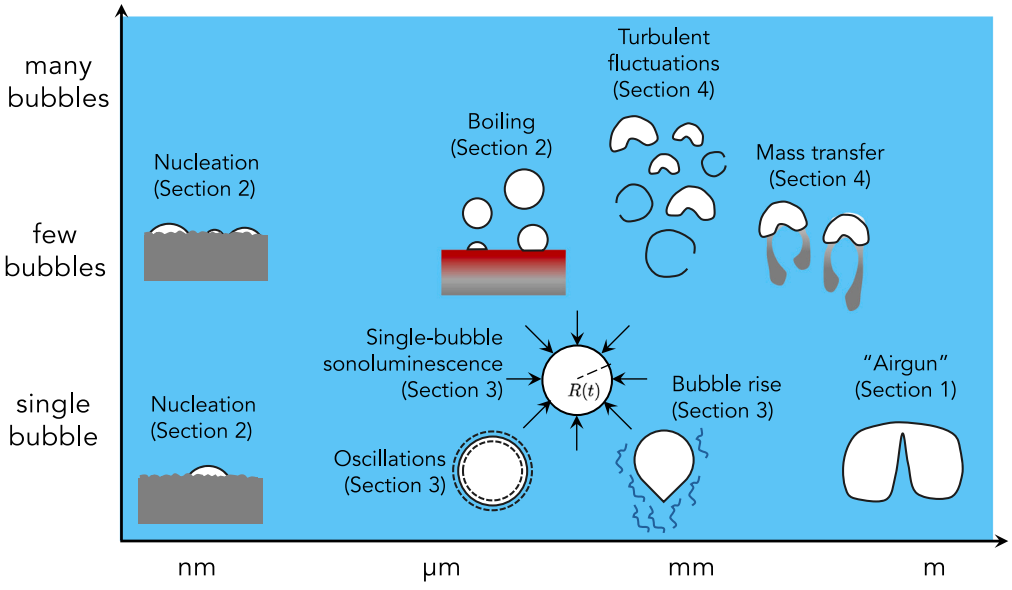

Fig. 1. Overview on the bubble phenomena discussed in this article, in the parameter space "number of bubbles" vs "length scale".

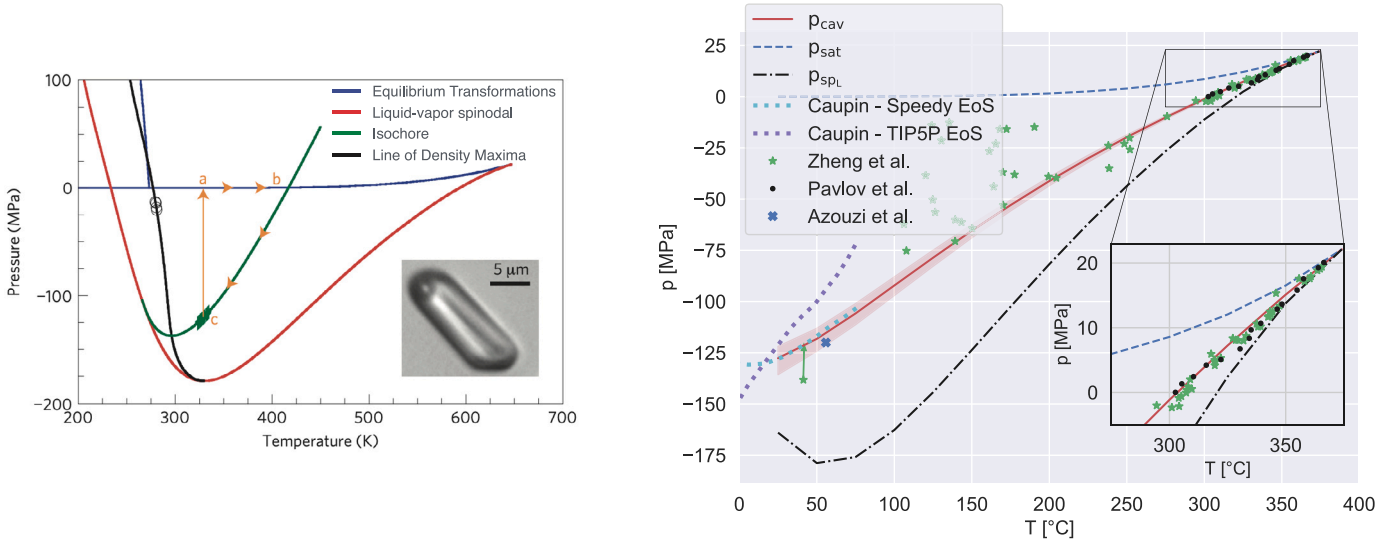

Fig. 2. Left panel: Nucleation in quartz micro-inclusions to estimate the tensile strength of water. Reproduced from Azouzi et al. (2013) with permission from Springer Nature. The experiment consists of a micrometer-sized cavity (see inset) filled with water. From the bi-phasic state – a – with liquid water and a vapor bubble, the system is warmed up along the liquid–vapor coexistence a – b. The bubble is fully adsorbed at the homogenization temperature b, whence the system is cooled along an isochore – the segment b – c. Suddenly the system snaps back from state c to state a where the original vapor bubble re-appears. From the bubble volume, a suitable equation of state allows inferring the pressure (Azouzi et al., 2013). The thickened portion of the green curve reports the cavitation temperature and pressure of 157 repeated experiments. The black open symbols are available experimental data on the Line of Density Maxima. Right panel: Cavitation pressure of water, computational results vs experimental data, Magaletti et al. (2021) and references therein. As explained in the text, bubble nucleation is a stochastic process. The symbols provide the experimentally determined cavitation pressure, namely the pressure where, for a given temperature, the probability of observing bubble nucleation is 1/2 given the system volume V and the observation time τ. The red solid line reports the prediction of the diffuse interface model, as explained in the text; the light red band shows the sensitivity when $V \cdot \tau$ varies in the range $1 - 10^6\,\mu m^3$ s. The dash-dotted black, and the dashed blue, lines show the spinodal and saturation pressures, respectively, as provided by IAPWS EoS. The inset is a zoom-in near the critical point.

2. Nucleation, cavitation and boiling

2.1. Definition of nucleation

Bubble nucleation consists of the appearance of a new gaseous phase in an otherwise homogenous liquid. For bubble nucleation to occurr, suitable thermodynamic conditions are needed, since liquid and gaseous states should coexist. In a pure, unbound liquid, the bubble is, classically, a spherical, vapor-filled cavity with a structureless, zero-thickness surface across which the fluid properties change abruptly. The bubble brings about a reduction of bulk-free energy but also implies the energy cost of forming the interface endowed with the surface tension γ. A critical radius $R_c = 2\gamma/\left(p_V - p_L\right)$ should be exceeded before the overall bulk and surface energy (grand potential) $\Delta\Omega = -\frac{4}{3}\pi R^3 \Delta p + 2\pi R^2 \gamma$ starts decreasing, where liquid and vapor pressure depend on temperature T and chemical potential μ, and $\gamma = \gamma(T)$. Neglecting the dependency of surface tension on the curvature radius, crossing the energy barrier, $\Delta\Omega^\dagger = 16\gamma^3/\left(p_V - p_L\right)^2$, requires energy, in some cases provided by external agents, like for high-energy particles inducing bubble nucleation in a water tank, enabling their detection. Most often, spontaneous energy focusing is due to thermal fluctuations, thus framing nucleation in the realm of thermally activated stochastic processes (Menzl et al., 2016).

The above description is very often too crude to encompass all the complexities of nucleation (Debenedetti, 2020), in particular in the cases relevant to applications. First, the energy barrier should vanish on approaching spinodal conditions, ruling out, strictly speaking, sharp interface models and calling, at least, for a small but finite thickness interfacial layer. Second, most commonly the liquid is not a pure substance. Dissolved gases are usually present and, particularly for polar fluids like water, impurities are unavoidable. The wettability and geometry of dust particles and bounding solids strongly influence bubble formation (heterogeneous nucleation). In most cases relevant to applications, gaseous nuclei remain trapped in wall crevices, which act as nuclei for the bubble nucleation (Atchley and Prosperetti, 1989), i.e., the nucleation is heterogeneous and not homogeneous. In other cases, the irregular geometry and wettability patterns act as catalysts, splitting the transition into partial steps, each associated with smaller energy barriers (Giacomello et al., 2013). Since the average time for nucleation depends exponentially on barrier height (Kramers, 1940; Blander and Katz, 1975; Menzl et al., 2016), $\tau \propto \exp\left[\Delta\Omega^\dagger/\left(k_B T\right)\right]$, this may explain why bubbles are easily formed in water, despite its large tensile strength (Azouzi et al., 2013; Magaletti et al., 2021), left panel of Fig. 2.

Surfactants reduce surface tension and, in extreme cases, can be so effective that the internal structure of the emerging interfacial layer manifests nonlinear elasticity and, possibly, even curvature elasticity effects (Rosen et al., 2005; Guido et al., 2016). The typical case of the former is found in surfactant-coated bubbles under strong and fast pressure oscillations (Marmottant et al., 2005). The latter was recently demonstrated in immiscible oil-water droplets, where the surface tension can be reduced to such a small amount to make the curvature elasticity dominant (Rosen et al., 2005; Guido et al., 2016).

The lead for Section 2.1 was taken by C.M.C.

2.2. Nucleation in boiling and cavitation: Nanoscale phenomena

A stable liquid can be brought into a metastable state by two conventional routes, namely by decreasing pressure at constant temperature – cavitation – or by increasing temperature at constant pressure – boiling.

Although induced by atomistic fluctuations, as pioneered by Van der Waals (1979), a mesoscopic description of nucleation can be envisaged starting with the (Helmholtz) free-energy

$$F[\rho, T] = \int_D \left[f_b(\rho, T) + \frac{1}{2}\lambda \nabla\rho \cdot \nabla\rho \right] \mathrm{d}V\,, \tag{1}$$

as functional of mass density and temperature, with f_b the free energy density of the homogeneous fluid of mass density ρ and λ being a capillary coefficient. The free energy functional can be exploited in conjunction with suitable rare events techniques (Ren et al., 2007) to determine the energy barrier and the minimum free energy path along

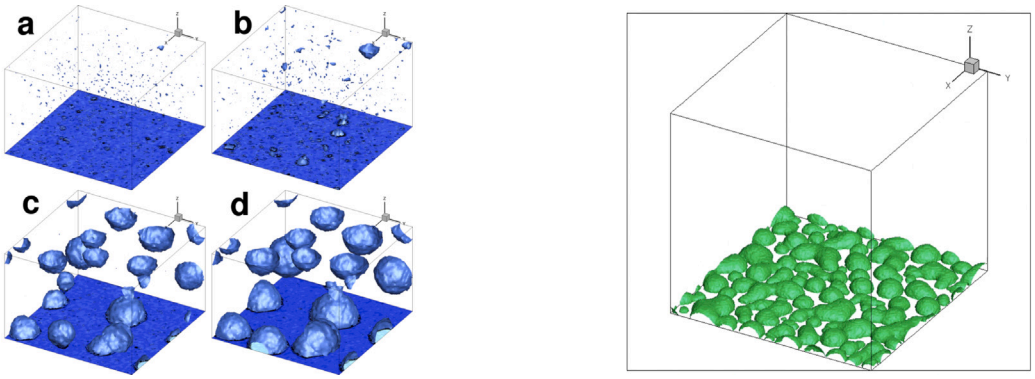

Fig. 3. Left panel: Four configurations during heterogeneous nucleation in a cavitating fluid in a slab between solid walls (Gallo et al., 2021). Bubbles are visualized by the critical density isosurface. The system is initialized in a homogenous metastable liquid state and the solid walls are neutrally wettable (equilibrium Young contact angle $\Theta_Y = 90°$). The equation of state corresponds to a fluid made of Lennard-Jones molecules (ϵ, σ, and m are the characteristic Lennard-Jones energy, length scale, and molecule mass with k_B the Boltzmann constant). As time advances, bubbles are progressively nucleated – $t/(\sigma\sqrt{m/\epsilon}) = 6 \times 10^4$ (a), 8×10^4 (b), 24×10^4 (c), 26.4×10^4 (d). At temperature $T = 1.25 \times \epsilon/k_B$ and liquid density $\rho_L = 0.475\, m/\sigma^3$ bubbles almost always nucleate at the solid walls. Right panel: Boiling onset under an imposed thermal flux from the lower wall (Gallo et al., 2023). A liquid in equilibrium with its vapor is heated from below at the lower solid, solid wall. The figure shows the bubbles formed at the heated wall at an instant along the transient. Bubbles are visualized by the critical density isosurface.

the liquid–vapor transition (Magaletti et al., 2021), see the right panel of Fig. 2 where the cavitation pressure of water is predicted. It is also the basis for deriving the distributed capillarity (Korteweg) stresses, in the spirit of nonequilibrium thermodynamics (De Groot and Mazur, 2013), leading to the system

$$\begin{aligned} \frac{D\rho}{Dt} + \rho\nabla\cdot\mathbf{u} &= 0\,, \\ \rho\frac{D\mathbf{u}}{Dt} &= -\rho\nabla\mu_g + \nabla\cdot(\boldsymbol{\Sigma}+\delta\boldsymbol{\Sigma})\,, \\ \rho\frac{De}{Dt} &= \nabla\cdot(\mathbf{T}+\delta\boldsymbol{\Sigma}) - \nabla\cdot(\mathbf{q}+\delta\mathbf{q})\,, \end{aligned} \tag{2}$$

where $\mathbf{u}$ is the velocity field, e the energy density, $\boldsymbol{\Sigma}$ the Newtonian component of the stress tensor, $\mu_g = \nabla\cdot\mathbf{T}_c = \delta F/\delta\rho$ the generalized chemical potential (functional derivative of the free energy) with $\mathbf{T}_c$ the Korteweg stress, $\mathbf{T}$ the (total) deterministic stress, and $\mathbf{q}$ the energy flux. Stress and the energy flux undergo fluctuations, $\delta\boldsymbol{\Sigma}$, $\delta\mathbf{q}$, modeled as zero average, Gaussian processes delta correlated in time with intensities determined by enforcing the fluctuation–dissipation balance, following Landau and Lifshitz's fluctuating hydrodynamics (Landau and Lifshitz, 1980). After augmenting the free energy functional with surface contribution allows the interaction with walls of different wettability (Gallo et al., 2021). The above system of stochastic PDEs allows the ab-initio direct simulation of the nucleation process under pressure decrease (cavitation) (Gallo et al., 2018, 2021) or temperature increase (Gallo et al., 2023) (boiling), see Fig. 3.

The size of the critical bubble is often comparable with the thickness of the interface, implying that bulk conditions are not obtained in the nucleus. Under these conditions, the interfacial forces may considerably differ from the equilibrium surface tension, an effect captured to first order in the curvature by the so-called Tolman correction (Tolman, 1949).

In the presence of solid walls, wettability plays a crucial role in determining the nucleation process, an effect crucial in addressing the onset of nucleate boiling (Gallo et al., 2023), with nucleation favored by hydrophobic surfaces.

The lead for Section 2.2 was taken by C.M.C.

2.3. Nucleation sites in boiling

Focusing now on heterogeneous phase change, nucleation sites are microscopic surface irregularities and cavities where stable vapor bubbles first form during boiling. Besides the liquid properties, these sites are influenced by surface characteristics, such as roughness, wettability, and its thermophysical properties. The activation of nucleation sites depends on the local temperature and pressure conditions, as well as the presence of dissolved gases or impurities (surfactants, nanodust and other) in the liquid and on the surface. Since it is not practically possible to exclude any impurity or small defects or presence of nanobubbles, the nucleation process, and therefore the heterogeneous boiling, is a stochastic process and large deviations of results in experiments are not only an issue due to a scarce attention in the experimental procedures, but also an evidence of the impossibility to take care of all the possible origins of nucleation at nanoscales.

Nucleation is at the basis for the characterization of boiling in terms of onset temperatures, heat fluxes, bubble generation rate and size, and so on (see the following paragraphs). The issue is that the standard boiling measurement are done at macroscale and only sometimes at microscales (Qi and Klausner, 2005; Marie et al., 2022; Stojanović et al., 2022), while bubble nucleation occurs at a scale 3–4 orders of magnitude smaller. Therefore, before trying to quantify macro-parameters such as the density number of visible nucleation sites, we need to deeply understand the nature of nanoscale nucleation. At macroscales it is very well known that surface roughness and wettability are extremely important parameters for nucleation in boiling (Hsu, 1962; Wang and Dhir, 1993; Bourdon et al., 2012, 2015). However, when the observer is zooming in towards the nanoscale level, the situation becomes less clear. We can consider as an example of the complexity to explore the nanoscale origin of boiling, the standard "Classical Nucleation Theory" (CNT), which we had explained in Section 2.1 and which provides a standard, application-oriented theoretical framework to describe the formation of a new phase (e.g., a liquid droplet in a supersaturated vapor or a solid particle in a supercooled liquid) from a parent phase. However, its predictions are often in contradiction to accurate experiments (Nam and Ju, 2008; Lefèvre et al., 2022). There are however other similarly accurate experiments (Witharana et al., 2012) which show that using a combination of a clean test rig and non-invasive data acquisition techniques, the bubble nucleation temperature of cavities and posts with sizes in the nano- to micro-scale range can be indeed described by CNT. In the work of Bao et al. (2017) the measured surface temperature for bubble nucleation is very close to the spinodal temperature for a wettable surface in a nanofluidics systems. Many experiments showing low onset temperature might have been affected by a poor control of the variables at nanoscales, but also the affirmation that CNT is still valid at nanoscale, when it is very clear that CNT is limited in many respects, seems quite stretched.

Indeed, there are various assumptions which the CNT makes, namely:

1. The surface tension of the critical nucleus is the same as that of a macroscopic interface. However, at the nanoscale, surface tension can vary significantly due to the curvature of the interface and the discrete nature of molecules (Popinet, 2018). The change of definition of the surface tension due to stretches of surface curvatures in the fundamental Gibbs' equation for the internal energy, results in a relevant variation of the onset temperature (Schmelzer, 2001). Once the corrected surface tension (for example, using the Tolman length) is considered in the CNT, good predictions of the boiling onset temperature can be recovered using advanced numerical analysis (Gallo et al., 2023). Studies have shown that the surface tension of small clusters can be size-dependent, which CNT does not account for (Lohse and Zhang, 2015).
2. CNT assumes that nuclei are spherical in shape, which simplifies the mathematical formulation but does not always reflect reality. In practice, nuclei can adopt various shapes depending on the anisotropy of the surface tension and the interaction with the surrounding environment (Matsumoto and Tanaka, 2008).
3. CNT uses bulk thermodynamic to describe the formation of nuclei. For very small clusters, these bulk properties may not be accurate, as small clusters exhibit different physical and chemical properties compared to the bulk phase. Molecular-scale effects, such as the discreteness of molecules and surface reconstruction, are not captured by CNT (Bartell, 2001).
4. CNT primarily focuses on the thermodynamic aspects of nucleation, often neglecting kinetic factors that can influence nucleation rates. Factors such as the diffusion of molecules to the nucleus, the attachment kinetics, and the presence of metastable states are not explicitly considered (Kashchiev, 2000).
5. CNT is derived under the assumption of relatively low to moderate supersaturation levels. At very high supersaturation levels, the assumptions of CNT, such as the equilibrium between the nucleus and the surrounding phase, break down (Laaksonen et al., 1995).
6. CNT is not considering the fact that bubbles under the critical radius can be casually generated very close to each other, and, in case of coalescence, once they are together they can reach the critical radius and grow: the space and time probability to find bubbles under a critical radius in a close neighborhood is therefore important (Magaletti et al., 2020).

Given the various obvious limitations, it appears very odd that the standard CNT can be generally valid for nanoscale nucleation and comparison with experimental data. Possible answers to this debate can come from one side from experiments at nanoscales (Paul et al., 2020; Zhong et al., 2020), which in turn are very difficult and create further questions. For example, in the work of Paul et al. (2020) the effect of the electromagnetic field and small defects of the pore may have an impact on nucleation, but this effect is not described. Therefore, when dealing with a quantification of the nucleation process for boiling, we still rely on the counting of microscopic bubbles on the surfaces (Hibiki and Ishii, 2003; Li et al., 2018; Cavicchi and Avedisian, 2007; Chang and Ferng, 2019), except for very particular experiments (Batchelor et al., 2021).

When considering simulations of the boiling process that include nucleation phenomena, several tools can be utilized: Classical Molecular Dynamics (MD) (Shahmardi et al., 2021; Liu et al., 2020; Yan et al., 2020; Ran and Bertola, 2024), including Coarse-Grained (Zipoli et al., 2013) and Metadynamics (Salvalaglio et al., 2016) methods, Density Functional Theory (DFT) (Lutsko, 2008), and Phase Field Methods, provided that they are augmented by Fluctuating hydrodynamics (Marengo and Coninck, 2022) or other schemes with which nuclei can be created. Effective, purely deterministic approaches focused on macroscopic scales may also approximately account for nucleation (Badillo, 2012; Haghani-Hassan-Abadi et al., 2021), assuming that phase change occurs right at spinodal conditions, where the nucleation barrier vanishes. Nanoscale effects are however always relevant for the onset since the actual phase change anticipates the spinodal, see Fig. 2(a) for the strictly related case of cavitation. Fluctuating Hydrodynamics integrates random fluctuations into fluid dynamics equations, capturing thermal fluctuations and noise in nucleation processes at nanoscales. These tools hold great promise for enhancing our understanding of nucleation processes, but they are challenging to scale to larger domains (even for a micrometer scale) due to the enormous computational requirements. Additionally, phenomena related to low nucleation rates, such as those near saturation temperatures far from the critical point, are difficult to simulate because the nucleation events occur too slowly relative to the necessary time steps for convergence. Enhanced Sampling Techniques like Parallel Tempering and Umbrella Sampling have been refined to better sample rare events in nucleation processes (Abrams and Bussi, 2014). However, these techniques are not yet suitable for a significant leap to larger scales. Conversely, computational methods for boiling that do not consider nucleation and nanoscale phenomena still rely on empirical, tunable parameters, such as the presence of a bubble seed or a specific threshold for temperature and heat flux at the surface (Kharangate and Mudawar, 2017; Chen et al., 2024). Therefore, multiscale modeling, which combines various simulation techniques to bridge different scales from quantum mechanical descriptions to continuum models, has gained increasing interest (Jiang et al., 2023). This approach provides a more comprehensive understanding of liquid–vapor phase-change processes. Recent applications in multiscale modeling of nucleation and growth in phase transitions are highlighted in Chen et al. (2024), Gennari et al. (2024). In this context, integrating machine learning with traditional simulation methods has significantly accelerated and improved the accuracy of liquid–vapor phase change studies. Neural network potentials trained on DFT data can achieve near-DFT accuracy with MD-level efficiency. Recent studies by Zhang et al. (2018) and Noé et al. (2020) have demonstrated the potential of deep learning in molecular simulations, showing significant improvements in predicting phase behavior and dynamic properties.

The lead for Section 2.3 was taken by M.M.

2.4. Bubble growth and detachment

After the nucleation of a vapor bubble on a wall or in the liquid bulk, it either grows or collapses. Regarding bubble growth, the initial stages are controlled by dynamic effects due to the overpressure inside the bubble. A linear evolution of the bubble radius with time $R \propto t$ can be obtained by integrating the Rayleigh–Plesset equation from the bubble's interface to the liquid far away. As the bubble expands, the internal pressure decreases, until it reaches the saturation pressure. A second mode of growth takes place, controlled by heat diffusion through the thermal boundary layer developing around the bubble. Analytical expressions are provided for the diffusive bubble growth in a quiescent liquid (Plesset, 1953; Scriven, 1959) where the bubble radius evolves as $R \propto t^{1/2}$. When heat transfer is controlled by advection around the bubble, the Nusselt number is function of the Plesset number $Nu \propto Pe^{1/2}$ and the bubble radius evolves as $R \propto t^{2/3}$ (Ruckenstein and Davis, 1971; Legendre et al., 1998). A general expression including the asymptotic bubble growth rates (inertial at short time and diffusive at long time) is given by Mikic et al. (1970).

The growth of vapor bubbles on a heated wall is more complex. It is controlled by evaporation at the interface in the superheated boundary layer and recondensation at the bubble top in subcooled liquid, as well as transfers in the vicinity of the wall. It has been extensively studied and numerous correlations for the bubble radius evolution are documented in text books (Carey, 2018). In a pioneer work, Cooper and Lloyd (Cooper and Lloyd, 1969) studied the growth of a vapor bubble in an organic liquid on a heated surface, highlighting the presence of a micro-layer beneath the growing bubble. As the

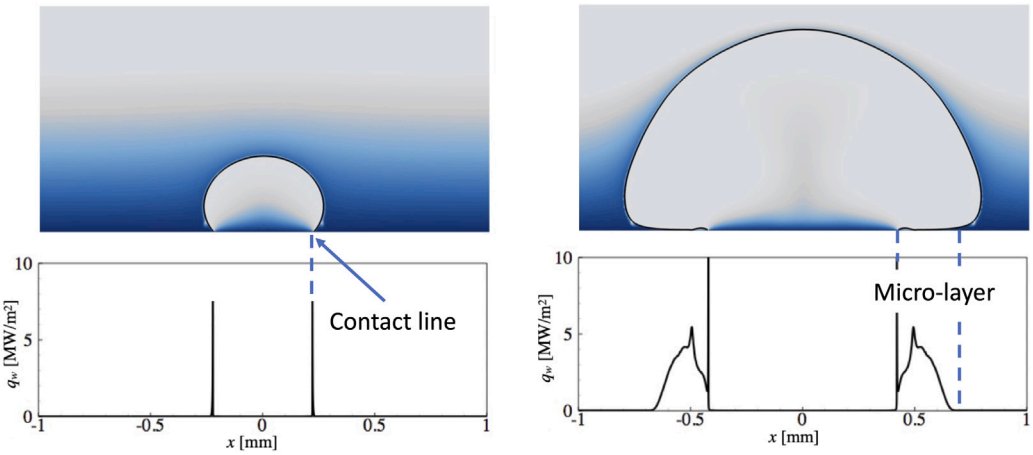

Fig. 4. Bubble growth in the contact line regime (left) and in micro-layer regime (right), bubble shape and heat flux distribution. Adapted from Urbano et al. (2018) with permission from Elsevier.

bubble interface velocity exceeds the dewetting velocity of the liquid on the surface, a thin micro-layer forms. They proposed an expression of the bubble growth rate based on the evaporation of this micro-layer. Recent experiments have been performed with advanced diagnostics based on high-speed visualization, infra-red thermography of the wall temperature and laser or white-light interferometry measurements to characterize the formation and depletion of this microlayer (Jung and Kim, 2018; Fischer et al., 2015; Wang et al., 2023; Tecchio et al., 2024). Typically, the micro-layer has been observed to be of a few micrometers thick and hundreds micrometer long, especially at low pressure and high wall superheat. Tecchio et al. (2024) showed that the microlayer can be seen as the Landau–Levich film deposited by the bubble foot edge.

In other experiments (Sodtke et al., 2006), the formation of the micro-layer has not been detected. This occurs particularly at low wall superheat and low bubble growth rate, where the interface velocity is lower than the dewetting velocity. However, even in absence of a micro-layer, an intense heat transfer is observed in the vicinity of the contact line. In Fig. 4, the two modes of bubble growth and the associated heat transfer q_w are plotted. The length of the micro-region is typically smaller than 0.1 micrometer. Within this region the increase in the interface curvature is linked to the intense liquid evaporation. Several models have been proposed to compute the heat transfer and a macroscopic contact angle at the edge of the microregion for fully wetting liquid (Stephan and Busse, 1992) or partly wetting liquid (Janecek and Nikolayev, 2012; Rednikov and Colinet, 2013). These models introduce an interfacial resistance based on an unknown accommodation coefficient. Such model could benefit from molecular dynamic simulations advances. The bubble growth in contact line regime has been especially studied thanks to microgravity experiments allowing for the observation of larger bubbles over extended periods (Sielaff et al., 2022) and thanks to direct numerical simulations (Son et al., 1999; Kunkelmann and Stephan, 2010; Huber et al., 2017). Recent numerical simulations emphasize the importance of integrating a micro-region model coupled with heat conduction in the wall to compute the bubble growth, particularly for wall with high thermal conductivity (Torres et al., 2024).

Since the bubble growth rates are very different in contact line and microlayer regimes, several authors have tried to characterize the transition between these 2 modes, either experimentally (Schweikert et al., 2019) or through direct numerical simulations (Urbano et al., 2018; Bures and Sato, 2022). This transition is similar to the Landau–Levich transition observed for adiabatic liquid films. Using the Cox–Voinov law, Bures and Sato (2021) derived a criterion for this transition, which depends on the contact angle at the edge of the microregion θ_{mr} and a capillary number based on the contact line velocity U_{CL}:

$$\theta_{mr}^3 \leq 9\ln(S)\frac{\mu U_{CL}}{\sigma}, \tag{3}$$

where S is the ratio of a macroscopic length scale of the microlayer and the length scale of the microregion.

Due to its complexity, heterogeneous bubble nucleation can be very counterintuitive.Wang et al. (2018) showed that plasmonic bubbles, which nucleate and then grow at a gold nanoparticle massively heated with a laser thanks to the plasmonic resonance, become larger for weaker heating and in degassed water: This is indeed extremely surprising on first sight, as one would expect larger vapor bubble for more laser power and larger bubbles more gas is dissolved, which would add to the vapor. These authors could quantitatively explain their findings by realizing that an early bubble nucleation (helped by dissolved gas and by very strong laser power) lead to a shorter delay time τ_d between turning on the laser and the actual bubble nucleation, leaving less time for the heating and therefore less time to dump energy into the system, and thus ultimately resulting in smaller vapor bubbles. The mechanism is explained in Fig. 5.

Next, we come to the prediction of the bubble detachment diameter which is a crucial issue for the prediction of the mass, momentum and energy transfer between the wall and the liquid bulk. Bubbles may detach under the effect of buoyancy or hydrodynamic forces. In a pioneer work, Fritz (Fritz, 1935) derived an analytical expression of the maximum volume of a gas or vapor bubble detaching from an horizontal wall under buoyancy. Numerous correlations mainly based on experiments can be found in Carey's book (Carey, 2018). Over the past thirty years, force balance models have been classically employed to predict bubble detachment (Zeng et al., 1993; Thorncroft et al., 2001; Van Helden et al., 1995; Situ et al., 2005; Colombo and Fairweather, 2015; Mazzocco et al., 2018). In flow boiling, bubbles can depart from the nucleation site and slide on the wall before detaching and lifting off or they can directly lift-off without sliding. Sliding is mainly observed on vertical wall. The forces (see Fig. 6) acting for the bubble detachment are buoyancy F_B, drag force F_D in the flow direction, lift force F_L perpendicular to the wall and contact pressure force F_{CP} due to the over pressure inside the bubble promotes the detachment (Thorncroft et al., 2001). The primary force keeping the bubble attached to the wall is the capillary force F_C which acts at the contact line. The capillary force may be affected by the surface wettability (Allred et al., 2021) (microscopic contact angle) but also by the evaporation at the contact line that strongly bents the interface. In the evaluation of this force, the apparent advancing and receding contact angles have to be considered. Additionally, as the bubble

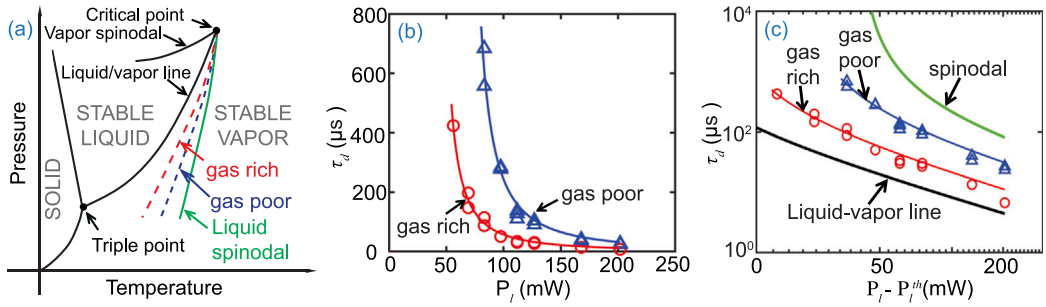

Fig. 5. Figure explaining the counterintuitive findings for plasmonic bubble nucleation and growth: (a) Phase diagram of water (schematics). The green solid line is the liquid spinodal line, the theoretical limit of superheat, while the blue and red dashed lines schematically depict the attainable superheat for gas-poor and gas-rich water. (b) Measured delay τ_d of bubble nucleation after the laser had been turned on, as function of the laser power P_l. The symbols represent the experimental data and the solid lines a fit curve based on the heat conduction equation. (c) Double logarithmic plot of the measured delay time τ_d vs $P_l - P_{th}$, where P_{th} is the threshold of plasmonic bubble nucleation. Both curves fall within the theoretical limits, namely the boiling temperature (black curve) and the spinodal curve (T_s = 578.2 K for a pressure of 1 atm, green curve). The shorter delay time τ_d for gas-rich water indicates that dissolved gas facilitates bubble nucleation. Reproduced from Wang et al. (2018).

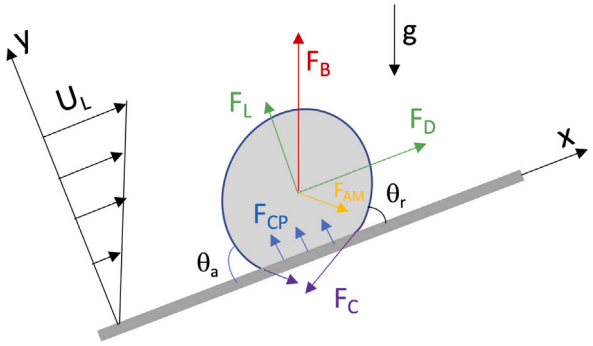

Fig. 6. Forces acting on a bubble during its growth on a wall.

growth rate is high, bubbles experiences an added mass force F_{AM} (Van Der Geld, 2009). The bubble departure or detachment is often predicted when the force balance in one direction becomes positive: $\Sigma F_x \geq O$ for sliding in the flow direction and $\Sigma F_y \geq O$ for lift-off perpendicular to the wall (Mazzocco et al., 2018). In most of the studies, all along the bubble growth, the force balance is often not assessed due the lack of knowledge about drag and lift forces for deformed bubbles attached to the wall in a shear flow, especially for a large range of bubble Reynolds numbers 10 to 500. Estimating capillary force is also challenging, since the bubble foot radius and the contact angles are not always precisely measured. Recently Favre et al. (2023) successfully assessed the force balance for truncated spherical bubbles growing on their nucleation site and sliding along a vertical wall for several experiments at different pressures. They used drag and lift coefficients obtained from direct numerical simulation of a spherical bubble in shear flow near the wall by Shi et al. (2020), and by taking into account the uncertainty in the estimation of the capillary force. The bubble detachment by sliding along the wall is directly linked to the motion of the contact line, as a critical value of the advancing contact angle θ_a is reached. Therefore, it is therefore more relevant to establish a criterion for bubble detachment based on a maximal value of θ_a instead of a criterion based on the imbalance of forces. Criteria based on the maximum advancing contact angle have been successfully applied to predict the detachment of air bubbles in a shear flow (Duhar and Colin, 2006). Another challenge is predicting the lift-off diameter of the bubble from a vertical wall, for which current models are unsatisfactory. In this configuration, the coalescence of bubbles also may be responsible for their detachment, inducing them to jump from the wall.

The lead for Section 2.4 was taken by C.C.

2.5. Heat transfer in nucleate flow boiling

Numerous correlations for the prediction of heat transfer in nucleate pool and flow boiling can be found in text books (Carey, 2018; VDI, 2010; Collier and Thome, 1994). Their validity is often limited to a restrictive range of parameters (tube diameter, fluid, mass flow rate, heat flux, quality..). Since the 1990s, Heat Flux Partitioning models (Kurul and Podowski, 1991) have been developed. The total heat flux q_w is divided into three contributions $q_w = q_{ev}+q_{conv}+q_{quenching}$. q_{ev} is the heat flux due to the evaporation of the liquid at the bubble foot or through the micro-layer. $q_{quenching}$ is the heat flux transmitted to the liquid after the bubble detachment, by transient conduction through the cold liquid replacing the bubble at the wall. q_{conv} is the heat flux transmitted to the liquid phase by convection between the bubbles on the surface. This HFP models are now classically used as boundary conditions in CFD codes for the prediction of boiling flows (Guelfi et al., 2007; Gilman and Baglietto, 2017; Amidu et al., 2020). They have the advantage to separate the heat flux transmitted to the liquid phase $q_{conv} + q_{quenching}$ and the heat flux generating vapor production q_{ev}. The modeling of the three contributions is based on local physical mechanisms and requires several closure laws such as bubble detachment diameter, bubble growth rate, frequency of detachment, density of nucleation site. Over the years, these models have been enriched, taking into account additional phenomena as bubble sliding on the wall, bubble coalescence, condensation at the bubble top (Warrier and Dhir, 2006; Zhou et al., 2021; Gilman and Baglietto, 2017). They have become more complex, requiring new closure laws. Continuous improvement of synchronized measurements techniques (high-speed visualizations, infrared thermography, interferometry) (Richenderfer et al., 2018; Zupancic et al., 2022) and direct numerical simulations (Sato and Niceno, 2018; Chen et al., 2022) provided valuable data for model improvement. The control of the density of nucleation sites on a surface by laser surface texturing (Zupancic et al., 2022) or chemical treatment is very promising for the improvement of heat transfer coefficient in nucleate boiling.

The lead for Section 2.5 was taken by C.C.

3. Single bubble phenomena

3.1. Rising bubbles and effective forces on bubbles

The simplest building block of bubbly flow is a single rising bubble in still water. It is a canonical and classical problem of fluid dynamics, which in spite of its simplicity can display extremely complex behavior, which could only be explained a few years back. Already Leonardo da Vinci realized that a small rising bubble in still water moves up straight, whereas a larger one in general spirals, see Fig. 7a. Due to this early reference to this phenomenon, Andrea Prosperetti has suggested

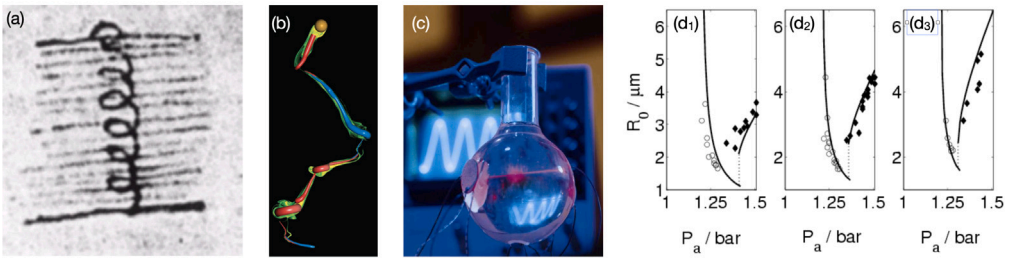

Fig. 7. (a) Leonardo da Vinci's drawing of a rising bubble. Taken from Fol. 25r, Codex Leicester. (b) Visualization of the vortex behind a rising sphere. Figure reproduced from (Horowitz and Williamson, 2010) with permission from Cambridge University Press. (c) Stable single bubble sonoluminescence: An acoustically trapped and strongly enough driven gas bubble can emit light. Figure taken from (Brenner et al., 2002) (d) Parameter space of single bubble sonoluminescence for a bubble in water with an air saturation of 10% (d_1), 20% (d_2), and 40% (d_3). The frequency of the driving sound is $f = 33.4$ kHz. P_a is the driving pressure amplitude and R_0 the resulting bubble radius. Solid lines show the theoretical parameter-free prediction; the right branches are for stable light emitting bubbles and the left branches for stable, non-emitting bubbles. The closed and open symbols show the corresponding experimental data from Ketterling and Apfel (1998). Reproduced from Toegel and Lohse (2003) with permission from AIP Publishing.

to call it Leonardo's paradox (Prosperetti, 2004), a name which has prevailed, though meanwhile we know that the transition is caused by an instability of the coupled system made of the bubble and the surrounding vortical flow (Mougin and Magnaudet, 2002; Tchoufag et al., 2014a,b). The instability mechanism results from the hydrodynamic fluid-body coupling made possible by the unconstrained motion of the bubble that behaves as a rigid, nearly spheroidal body on the surface of which water slips freely (Ern et al., 2012; Bonnefis et al., 2023, 2024). We emphasize that also rising or falling spheres can experience a path instability towards a zig-zagging or spiraling rise mode once the Galileo number is large enough (Veldhuis et al., 2005; Horowitz and Williamson, 2010; Ern et al., 2012).

We note that even in still water a bubble need not rise, but can sink! Of course, then extra forces are at play. This could be acoustical forces or – as in the famous example of Young et al. (1959) – thermal Marangoni forces. In that paper the author set up a stably stratified temperature gradient in a liquid such that the surface tension of a gas–liquid interface at the top is larger than at the bottom. For water this is possible for liquid temperatures below 4 °C due to the density inversion at those temperatures. Once a bubble is injected, the larger surface tension at the top of the bubbles pulls liquid along the bubble's interface from the bottom to the top, leading to a downwards Marangoni force which can overwhelm the upwards gravitational forces.

Once the bubbles are small enough, the forces on them can quite well be described with point-particle approaches, in the spirit of what Maxey and Riley have done for small particles (Maxey and Riley, 1983). A very nice summary of these forces has been given by Magnaudet and Eames (2000). Next to buoyancy, drag, and the added mass force, the lift force can be very crucial. The key question then is: How do drag, lift, and added mass coefficient depend on the bubble size, the possible bubble deformation, and the local flow parameters? This concept can also be extended to include acoustic forces or Marangoni forces.

3.2. Single-bubble sonoluminescence

Even simpler than a single rising bubble is a single *trapped* bubble. This can be achieved by acoustic forces in a standing acoustic field, the so-called Bjerknes forces of the first kind. Bubbles levitated in this way are ideal for the study of the radial bubble dynamics, their shape instabilities, and for the analysis of diffusive fluxes into and out of the bubble. If acoustically driven very strongly, remarkably, such trapped bubbles can emit light, see Fig. 7c. This phenomenon, called stable Single bubble sonoluminescence (Brenner et al., 2002), was first found in 1990 by Felipe Gaitan, then a Ph.D. student in the group of Larry Crum (Gaitan, 1990; Gaitan et al., 1992). It is pretty remarkable as acoustical energies are in the range of 10^{-12} eV/molecule, whereas visible light (emitted photon) in the range of 1 eV/molecule. The observation of the phenomenon triggered various wild speculations, but within less of a decade after its discovery it could quantitatively be explained as a beautiful example of – literally speaking – illuminated bubble dynamics.

As Brenner, Hilgenfeldt, and Lohse could show, four conditions must be fulfilled for stable single bubble sonoluminescence to occur: (i) Shape stability of the bubble, (ii) diffusive stability of the bubble (Hilgenfeldt et al., 1996), (iii) chemical stability of the bubble (which requires the presence of inert gases like argon, contained in air at a concentration of 1%) (Lohse et al., 1997), and (iv) strong enough energy focusing at bubble collapse so that the gas inside the bubble can heat up to such a degree that it partially ionizes; the light emission then occurs as thermal bremsstrahlung at recombination of the electrons and the ions (Hilgenfeldt et al., 1999). By putting together the above four criteria, a quantitative and parameter free prediction of when stable single bubble sonoluminescence can be achieved is possible, which is in excellent agreement with the experimental data, cf. Fig. 7d. Single bubble sonoluminescence is reviewed in great detail in Ref. (Brenner et al., 2002). The present overview article does not allow to go into the details, but we thought that it would be useful to mention the phenomenon, whose quantitative explanation turned out to be a triumph for classical bubble dynamics, as developed by Prosperetti and Plesset in the 60s, 70s, and 80s of the last century (Prosperetti, 1977b; Plesset and Prosperetti, 1977; Prosperetti, 1977a; Prosperetti et al., 1988). In this sense, again, single bubble sonoluminescence is nothing else but illuminated bubble dynamics.

The lead for Sections 3.1 and 3.2 was taken by D.L.

3.3. Bubble rise in viscoelastic media

Many applications in biotechnology, bio-process engineering and polymer processing involve bubbly flows in rheologically complex liquids. For predicting the transport rates of heat and mass across the bubble surface in order to quantify the intensity of the processes – together with the residence time of the bubbles in the liquid – the bubble dynamics must be known in detail. Since the pioneering work by Astarita and Apuzzo (Astarita and Apuzzo, 1965) it has been known that single bubbles rising in quiescent viscoelastic liquids may exhibit a jump discontinuity of their rise velocity depicted as a function of the bubble volume. Supercritical bubbles rise up to an order of magnitude faster than subcritical ones, see Fig. 8(a) for an example, where the steady state bubble rise velocity is given as function of the bubble volume for various polymeric concentrations w (given in mass percent).

Both the critical bubble volume and the increase of the bubble velocity at the jump discontinuity depend on the material properties of the liquid. Astarita and Apuzzo showed that for a shear-thinning viscoelastic liquid, the ratio of the terminal rise velocities just above and below the critical volume can be much larger than the well-known factor of 1.5, which appears in the Newtonian case at the transition from the Stokes to the Hadamard–Rybczynski regime. They furthermore reported this jump in the bubble rise velocity to be accompanied

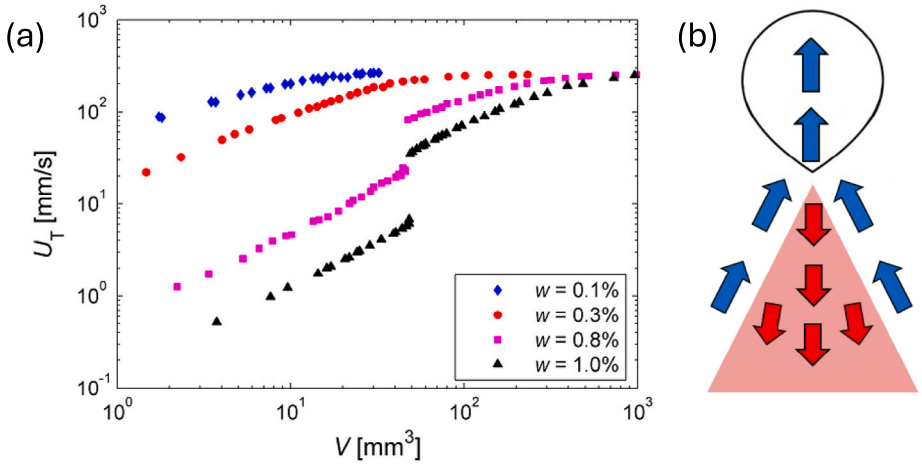

Fig. 8. (a) The steady-state rise velocity of individual air bubbles in various aqueous poly(acrylamide) solutions as a function of the bubble volume. The polymer content w is given in mass fraction percent. Reprinted from Pilz and Brenn (2007) with permission from Elsevier. (b) Structure of the wake of a supercritical bubble rising in a viscoelastic liquid. Adapted from Funfschilling and Li (2001).

by a change in the bubble shape from a convex to a "teardrop"-shaped surface. As a possible explanation, the authors suggested that the jump of the bubble rise velocity corresponds to a change of the interfacial properties from rigid to free. This switch in the boundary conditions at the bubble surface would result in a transition similar to the one for a Newtonian liquid.

One further important property of the flow field around supercritical bubbles is an unexpected structure of the wake, discovered by Hassager (Hassager, 1979). For solutions of a polymeric substance in a Newtonian solvent, the flow field around the bubble is structured in three distinct zones: an upward flow in front of the bubble, similar to that in the Newtonian case, a downward flow in the central wake, denoted negative wake by Hassager, and a hollow cone of upward flow enclosing the region of the negative wake. This structure is illustrated in Fig. 8(b). In their flow visualization measurements, employing Particle-Image Velocimetry (PIV) and birefringence, Funfschilling and Li (Funfschilling and Li, 2001) showed such flow fields around bubbles rising in aqueous polyacrylamide solutions. The birefringence visualization qualitatively revealed a butterfly-like spatial distribution of shear stress around the bubble within any plane through the axis of symmetry.

A large number of theoretical and experimental studies were carried out to find an explanation for this phenomenon. Characteristic numbers like the Bond number, the Capillary number and a non-dimensionalized normal stress in the liquid have been used in criteria for the occurrence of the jump discontinuity and the critical bubble volume. Pilz and Brenn studied experimentally the rise of individual air bubbles in viscoelastic solutions of different polymers in various solvents (Pilz and Brenn, 2007). Steady-state bubble rise velocities in aqueous solutions of a flexible poly(acrylamide) at different concentrations from (Pilz and Brenn, 2007) are shown in Fig. 8(a). From the experiments, a non-dimensional correlation for the critical bubble volume and for the potential of the polymeric liquid to exhibit the jump discontinuity were derived. Fraggedakis et al. (2016) numerically analyzed the velocity jump discontinuity, computing quasi-steady solutions of the governing equations for individual rising bubbles in a viscoelastic liquid. The setup of the experiments by Pilz and Brenn (2007) was reproduced numerically. For two different polymer concentrations, very good agreement with the experimental data from (Pilz and Brenn, 2007) has been obtained for the subcritical states of bubble rise, both concerning the rise velocity and the bubble shape. In a recent study, Bothe et al. (2022) identified the mean molecular deformation of the dissolved polymeric substance induced by the kinematics of the biaxial straining flow around the northern bubble hemisphere as responsible for the formation of a hoop stress in the azimuthal direction (Fig. 9a). The interplay between the molecular polymer deformation and the Brownian relaxation has been identified as the reason for the strong difference between the sub-critical and super-critical states of the bubble motion. While in the subcritical state the hoop stress in the azimuthal direction, formed by the polymer deformation, relaxes completely along the northern bubble hemisphere, the flow around the supercritical bubble transports the polymer molecules fast enough, hence still in a stretched state, down beyond the equatorial plane. The molecules therefore still relax while moving along the southern hemisphere, releasing their stored energy there, which acts as a push to the bubble in its rising direction. Subsequent polymer molecules hence reach the southern hemisphere faster, hence with more stored energy left. This induces a self-amplification, which leads to an abrupt increase in the rise velocity. At the same time, the forces transmitted to the bubble surface pinch the surface to the vertical axis of symmetry, thus resulting in a teardrop-like shape.

The molecular mechanism identified as the origin of the velocity jump discontinuity allows the formation of the negative wake to be explained together with the sub- or supercritical state of the bubble motion, too. The release of energy stored in the polymer molecules at the southern hemisphere of the bubble leads both to a force on the bubble supporting the rising motion, and also to the flow field leading to the negative wake. Numerical simulations allow the evolution of these flows in time to be predicted.

Future research shall use numerical simulations to explain further experimental findings reported in the literature. The experiments by Pilz and Brenn (Pilz and Brenn, 2007) indicated that a sharp bubble rise velocity jump discontinuity as found in solutions of flexible polymers (Fig. 8a) does not exist in solutions of rigid rod-like polymers. As a reason for this, the different mechanism of molecular relaxation was assumed. With flexible polymers in good solvents, the molecular relaxation bringing the molecules from a deformed molecular state to a random coil is due to Brownian motion. In contrast, with rigid rod-like polymers, relaxation is a process of rotational diffusion. Furthermore, the details of the negative wake formation induced by the molecular polymer relaxation in the supercritical case, to be explained by this same molecular mechanism, remain to be clarified quantitatively. Experiments by Pilz and Brenn (Pilz and Brenn, 2007) furthermore showed that, in solutions of rigid rod-like polymers, a negative wake can exist with subcritical bubbles as well. Yet, Harlen showed that a negative wake occurs behind rigid spheres settling in viscoelastic liquids (Harlen, 2002). The aim of this research should be to develop a universal explanation for the formation of the negative wake, accounting both for different (fluid or solid) bodies moving in the liquid, and

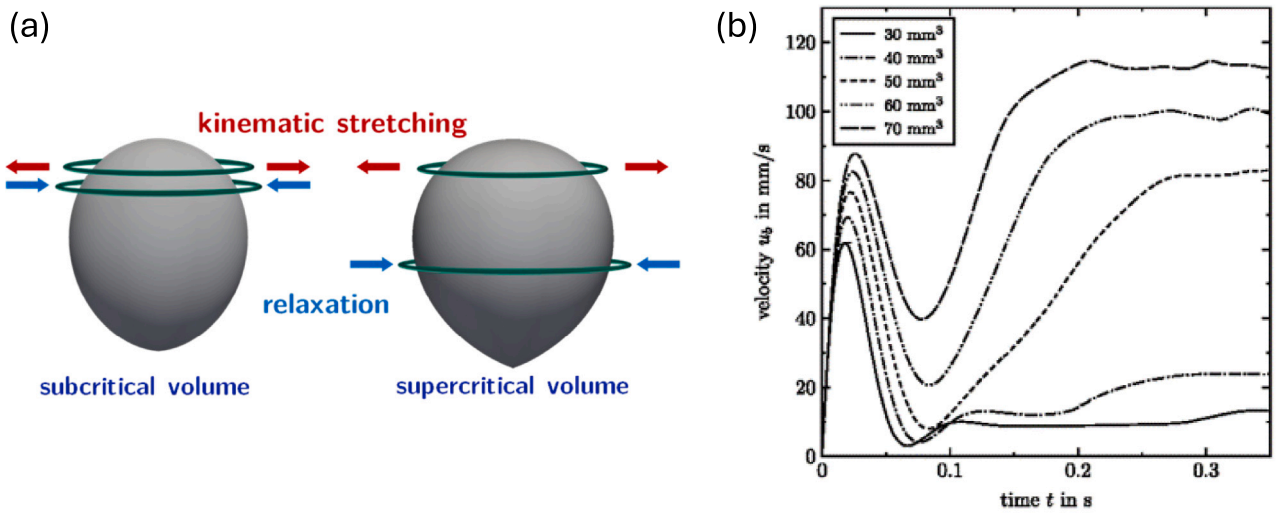

Fig. 9. (a) Principle of the mechanism of hoop stress formation and relaxation for subcritical and supercritical bubble volume. Reprinted from Bothe et al. (2022) with permission from Elsevier. (b) Evolution of the bubble rise velocity, starting from rest, in a viscoelastic fluid. Reprinted from Niethammer et al. (2019) with permission from Elsevier.

for different molecular properties of the liquid. Detailed simulations on the rise of individual bubbles in viscoelastic liquids should lead the way to an explanation of the genesis of the subcritical or supercritical states of bubble motion. Starting from rest, the velocities of bubbles with different volumes undergo evolutions as shown in Fig. 9(b). The simulations will allow the forces acting on the bubble to be identified as the reasons for the accelerated and decelerated states of bubble motion, which result in the terminal rise velocities. Understanding the non-monotonic transient rise behavior is the subject of ongoing research.

The lead for Section 3.3 was taken by G.B. and D.B.

3.4. Bubble dynamics in viscoelastic media

Next to bubble rise, the dynamics of bubbles undergoing spherical deformation in viscoleastic media is relevant for a broad range of applications (Dollet et al., 2019), from biomedical ultrasound (see Section 3.5) to the processing of materials and food products. The properties of a viscoelastic medium surrounding a bubble strongly affect the bubble dynamics. Similarly, surfactant molecules on a bubble surface (see Section 3.5) modify the bubble dynamics through the viscoelastic properties of the interfacial layer (Marmottant et al., 2005). The response to stress of a viscoelastic material can be highly nonlinear, and can therefore cause dramatic changes in bubble dynamics, which is in itself highly nonlinear even in simple fluids, as shown in the classical theory of bubble dynamics by Plesset and Prosperetti (1977).

The effect of a viscoelastic medium on bubble dynamics has been tackled over the past decades, for increasingly more complex and nonlinear response to stress of the medium, with the aim to both provide predictive models and to highlight qualitatively new behaviors. Theoretical studies have led the way. Similar progress has been made in mathematical modeling of the effect of a viscoelastic layer on bubble dynamics, which is not covered here.

The first models of bubble dynamics in viscoleastic media accounted for linear viscoelastic effects, which are valid for small-amplitude deformation of the material: the linear Maxwell model (Fogler and Goddard, 1970) and the Kelvin-Voigt model (Church, 1995) have been first combined with the Rayleigh–Plesset equation governing bubble dynamics. To account for the fact that complex fluids can have intermediate behavior between fluid and solid, these two models can be combined into the Standard Linear Solid model, which has been combined with the Keller-Miksis equation for bubble dynamics (Hua and Johnsen, 2013). To model relatively large deformations, the equation governing bubble dynamics can be combined with a non-linear constitutive model, valid for large strains, keeping in mind that compressibility effects can also become important for large deformation. Several authors have considered a non-linear version of the Maxwell model in the context of bubble dynamics (Allen and Roy, 2000; Jiménez-Fernández and Crespo, 2005; Naude and Méndez, 2008; Warnez and Johnsen, 2015); this model predicts aperiodic oscillations and chaotic behavior (Jiménez-Fernández and Crespo, 2005; Naude and Méndez, 2008), when the forcing period is much shorter than the relaxation time of the material, which causes the stress in the medium to build up cycle after cycle of oscillation. In the limit of predominantly solid-like materials, the effect of non-linear elasticity has also been analyzed (Gaudron et al., 2015). All of these models were recently combined into a single unifying equation, applicable for large bubble deformations in viscoelastic media (Oratis et al., 2024). Because in this model the medium rheology is formulated through a relaxation function, rather than a separate relaxation equation, this approach generalizes the Rayleigh–Plesset equation to materials with arbitrary complex rheology. Lastly, the behavior in viscoelastoplastic fluids (or yield-stress fluids), which behave as solid below a threshold and as liquid above it, has also gained increasing attention (Karapetsas et al., 2019; De Corato et al., 2019).

Experiments that can provide the same level of detail as these theoretical studies, such as time-resolved measurements of the radial dynamics of bubbles and resonance curves in complex fluids with controlled properties, have become possible more recently. The experimental data can then be fitted to a model combining the Rayleigh–Plesset equation with an appropriate constitutive model for the fluid, to extract its rheological properties (Saint-Michel and Garbin, 2020b). Oscillatory bubble dynamics, based on forced bubble oscillations of controlled amplitude and frequency driven by ultrasound, can provide measurements of rheological properties of viscoelastic media at high frequency (10^4–10^5 s^{-1}) (Jamburidze et al., 2017), see Fig. 10(a). Bubble collapse is also sensitive to the rheology of the surrounding medium (Estrada et al., 2018), see Fig. 10(b), and it gives access to high strain rates (10^7 s^{-1}) which are otherwise difficult to achieve with other methods. Experiments have gradually addressed more complex fluids, such as yield-stress materials (Saint-Michel and Garbin, 2020a), which become fluid under stress; and shear-thickening fluids (Bokman et al., 2022), which become solid under stress, such that a cavitation bubble causes fracture rather than deformation of the material, as shown in Fig. 10(c). These recent developments show that a strong bridge is being formed between the traditionally separate communities of bubble dynamics and cavitation on the one hand, and rheology on

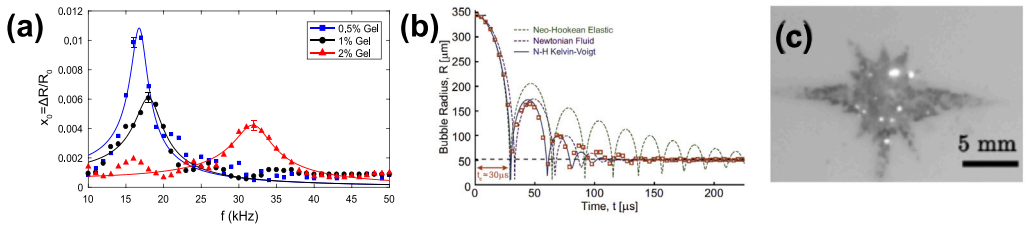

Fig. 10. Bubble dynamics in viscoelastic media. (a) Linear viscoelastic properties of hydrogels from linear resonance curves of oscillating bubbles. The shift in resonance frequency depends on the concentration of the gel and therefore its elasticity. Adapted from (Jamburidze et al., 2017) with permission from the Royal Society of Chemistry. (b) Experimental measurement of high-strain rate viscoelastic properties from bubble collapse. Adapted from (Estrada et al., 2018) with permission from Elsevier. (c) Cavitation-induced fracture in a shear-thickening fluid (cornstarch suspension). Adapted from (Bokman et al., 2022) with permission from the American Physical Society.

the other hand. This synergy will enable the continued development of methods that exploit our knowledge of bubble dynamics to probe and characterize complex fluids (Saint-Michel and Garbin, 2020b) and to manipulate soft materials, as described in the following section.

The lead for Section 3.4 was taken by V.G.

3.5. Bubbles in biomedical ultrasound applications

An important example of bubble dynamics in complex fluids and viscoelastic media is encountered in biomedical ultrasound applications. The use of bubbles and ultrasound is well established both for medical imaging and therapeutic applications (Coussios and Roy, 2008). In ultrasound imaging, the scattering of ultrasound by blood is enhanced by a contrast agent that consists of a suspension of microbubbles, typically 1-2 μm, stabilized against dissolution and coalescence by an interfacial layer of surfactants. The oscillatory dynamics of bubbles in ultrasound is exploited in different imaging protocols to image blood flow, thanks to the non-linear response of bubbles which makes them clearly visible while surrounding tissues mainly scatter sound linearly. Several microbubble formulations are clinically approved as contrast agents for ultrasound diagnostic imaging (Borden and Song, 2018) and the most advanced ultrasound imaging protocols can now detect single echoes from individual microbubbles in blood capillaries *in vivo* (Errico et al., 2015), as shown in Fig. 11(a). In therapeutic ultrasound, the use of microbubbles can increase the efficacy of thrombolysis (Tachibana and Tachibana, 1995), reduce acoustic power and treatment time in high-intensity focused ultrasound for tumour ablation (Jiang et al., 2014), and help deliver drugs at otherwise inaccessible locations, for instance across the blood–brain barrier (Choi et al., 2011). The stresses applied by bubble collapse or bubble oscillations then need to be controlled to optimize these procedures.

The flow field generated by bubble dynamics and the resulting stresses applied to cells are now relatively well understood for the case of *sonoporation*, which refers to the transient increase in the permeability of a cell membrane due to microbubble activity in ultrasound. Sonoporation can be caused by different mechanisms (Lentacker et al., 2014): on the one hand, the liquid jet caused by a collapsing bubble can induce a temporary pore into the cell membrane (Ohl et al., 2006; Helfield et al., 2016), see Fig. 11(b); on the other hand, a microbubble undergoing stable oscillations can cause sonoporation due to the shear stresses induced by microstreaming flow Fig. 11(c) (Pereno et al., 2018).

An emerging application of biomedical ultrasound is in neurostimulation, where cavitation is thought to occur at the sub-cellular scale: the cell membrane can absorb mechanical energy from an ultrasound wave, leading to bubble formation between the two lipid layers that make up the cell membrane (Krasovitski et al., 2011). Cavitation and bubble dynamics can in certain situations cause harmful bioeffects instead of being beneficial: for instance, cavitation due to a shock wave propagating in the brain is thought to play a role in traumatic brain injury (Adhikari et al., 2016).

It is then clear that, for these and many other medical applications of ultrasound, understanding and quantifying the stresses induced by bubble dynamics near or within soft materials, from the cellular scale to the scale of entire tissues, is crucial for controlling the outcome of a procedure.

The lead for Section 3.5 was taken by V.G.

4. Bubbly flows

4.1. Turbulent fluctuations in bubbly flows

Consider a population of dispersed bodies moving through a fluid, focusing on cases where inertia plays a major role. Whatever the nature of the bodies (gas bubbles, solid particles, liquid droplets) or the physical parameters, the flow undergoes random fluctuations. These fluctuations have various origins that need to be distinguished (Risso, 2018). On the one hand, the overall flow may be turbulent independently of the presence of a dispersed phase. In single-phase-flows, turbulence is generated by the gradients of the mean velocity, this Shear-Induced Turbulence (SIT) being modulated by the presence of a dispersed phase in two-phase flows (Balachandar and Eaton, 1984; Crialesi-Esposito et al., 2022). On the other hand, the motion of the dispersed phase relative to the carrying phase also generates fluctuations, referred to as Body-Induced Agitation (BIA), which itself involves two kinds of fluctuations (Riboux et al., 2013; Amoura et al., 2017). Each body generates a disturbance in its surroundings, which may include a boundary layer, a potential flow, and a wake, all contributions that depend on the presence of the other bodies. The collective contribution of those disturbances is named Local Body Disturbances (LBD). In addition, the flow of the continuous phase through the swarm of randomly dispersed bodies becomes turbulent provided the Reynolds number is large enough, which generates Body-Induced Turbulence. When the dispersed phase is homogeneously distributed over space, BIA mainly involves length scales of the order of the dispersed bodies or smaller.

A strategy to study turbulent dispersed two-phase flows may consist of studying homogeneous BIA before to investigate the interaction between BIA and SIT. Experimentally, homogeneous BIA can be produced by considering a swarm of bodies moving relative to a fluid at rest (or at constant average velocity) under the action of gravity, such as a bubble column (for gas–liquid systems) or a fluidized bed (for solid–liquid systems).

However, several mechanisms may cause the bodies to cluster, leading to the instability of the homogeneous case. It is therefore important to determine under which condition we can obtain a stable swarm of homogeneous bodies. A diagram of the various flow regimes of a column of air bubbles rising in water at large Reynolds number ($Re \geq 400$) is given in Fig. 12 for various gas volume fractions α. The velocity of an isolated bubble ($\alpha = 0$) shows wake-induced oscillations around an average rise velocity V_0 (Ellingsen and Risso, 2001; Zenit and Magnaudet, 2008). A few interacting bubbles can rise faster than V_0 because they minimize their overall drag. In general they form clusters (Martínez Mercado et al., 2010; Figueroa-Espinoza et al., 2018), so the flow involves several length scales: the bubble diameters d, the bubble wake length Λ, and the cluster size L_c. Increasing α, the

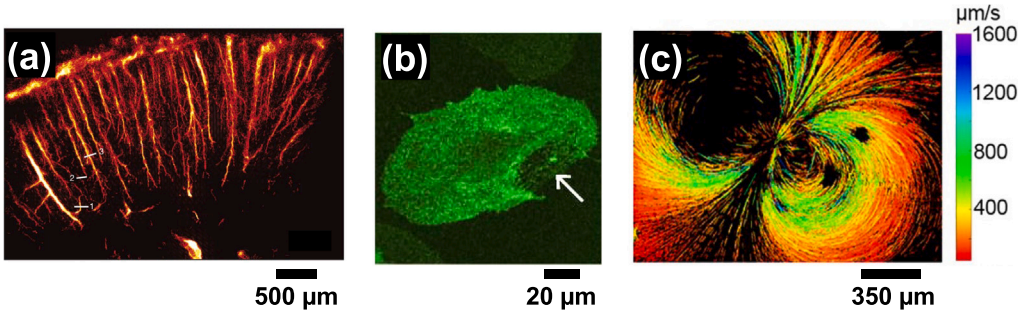

Fig. 11. Biomedical applications of ultrasound contrast agent microbubbles. (a) Ultrasound localization microscopy of blood capillaries *in vivo*. Adapted from (Errico et al., 2015) with permission from Springer Nature. (b) Fluorescence microscopy recording of sonoporation, highlighting a large pore in the cell membrane. Adapted from (Helfield et al., 2016). (c) Velocimetry measurements of microstreaming flow induced by commercial ultrasound contrast agent microbubbles. Adapted from (Pereno et al., 2018) with permission from AIP Publishing.

external fluid is forced to pass in the interstices between the bubbles, the drag increases and the bubble velocity V decreases; this is the so-called hindering effect.

When the bubble agitation is large enough to prevent cluster formation, we observe a true homogeneous regime where liquid fluctuations are dominated by bubble wakes (Riboux et al., 2010), with an energy that broadly evolves as αV^2 and a characteristic scale given by the bubble wake length, which is only of a few diameters because of the strong attenuation generated by the interaction between wakes (Risso et al., 2008). Then, above a certain α, the homogeneous state becomes unstable and clusters develop, leading to large-scale buoyancy-driven flows (Mudde, 2005), which may increase the gas velocity as the segregation Boycott effect competes with the hindering effect. Eventually, the size of the largest clusters reach the column width and the flow dynamics become totally controlled by the column diameter D. This is the pure heterogeneous regime that has recently be characterized by Mezui et al. (2022, 2023). The frontiers between those regimes depend on many parameters, but the pure homogeneous regimes is commonly obtained for volume fractions between 0.5 and 15%.

Note that a qualitatively similar behavior is observed for fluidized solid spheres in water, with a homogeneous regime where the average relative velocity between the two phases, V, decreases with the solid fraction Φ while the fluctuating energy increases as $\Phi(1-\Phi)V^2$ (Alméras et al., 2019); this regime being limited at low Φ by an instability of the bed whose onset depends on particle inertia, and at large Φ by the packing of the particles, close to $\Phi = 0.6$ for spheres (Amin et al., 2021). The investigation of such systems taught us that if LBD is present in any case, bubble induced turbulence (BIT) needs that it exists a large enough three-dimensional space between the bodies. For instance, in a rising swarm of bubbles confined between two close plates (Bouche et al., 2014), turbulence is prevented from developing due to the confinement. Similarly, in large-Re fluidized beds, the volume fraction is generally larger than 0.2 and the interstices are too narrow for the turbulence to develop (Alméras et al., 2021). In a three-dimensional bubble column at large volume fractions, as in the pure heterogeneous regime, the flow between the bubbles can also hardly become turbulent and it is the flow of the whole gas–liquid mixture that is turbulent, which is a very different mechanism of the BIT observed in the homogeneous regime. However, in a homogeneous three-dimensional bubble column ($0.01 \leq \alpha \leq 0.20$), the BIT plays a major role in the dynamics of the fluctuations.

BIT has been investigated for more than forty years in numerous experimental and numerical studies (Risso, 2018), which revealed its peculiar characteristics: exponentially decaying wakes; velocity fluctuations featuring anisotropic non-Gaussian Probability Density Functions with exponential tails; Velocity spectra exhibiting a k^{-3} regime starting from $2\pi/\Lambda$. However, it is only recently that numerical simulations have given access to spectral energy budgets (Pandey et al., 2020; Zamansky et al., 2024; Ramirez et al., 2024), necessary to understand turbulence mechanisms. Fig. 13a shows a typical example of such a budget obtained from DNS of a homogeneous swarm of rising bubbles by Ramirez et al. (2024). (We note that all terms show oscillations with a frequency $k_b = 2\pi/d$, which are due to the jump conditions of density and stress fields at interfaces. These oscillations can be suppressed by removing the irregular parts of the spectra by appropriate treatment, as described in Ramirez et al. (2024), and they will not be discussed further here.) Energy is supplied by the bubbles through the work of the buoyancy (green line) in the range from 0.2 to $2k_b$ with a peak near $0.7k_b$. It is transferred to larger k by the joint works of inertia (red line), as in single-phase flow, and interfacial forces (black line), which are specific to bubbly flows. Dissipation (blue line) peaks close to $k \approx k_b$ before to decay as k increases. There is no scale separation between production and dissipation and the budget evolves from a production/transfer equilibrium to a transfer/dissipation equilibrium. The famous k^{-3} subrange of the velocity spectrum corresponds here to a k^{-1} subrange of the dissipation, which starts after the production peak and continues along the transfer/dissipation range. The dynamics of this regime has been associated with the mean shear rate of the wakes and interpreted as a mechanism to return to isotropy by Zamansky et al. (2024).

In a swarm of rising bubbles, interfaces play thus a dual role: (1) generating fluctuating energy at scales close to the bubble size via the buoyancy-driven motion, and (2) transferring this energy to small scales via the work of interfacial forces. It is worth comparing this result with the case where the interfaces are not the cause of energy production. Fig. 13b shows the spectral energy budget obtained from the DNS of a swarm of droplets immersed in a Homogeneous Isotropic Turbulence by Crialesi-Esposito et al. (2022). As gravity is not taken into account, there is no average movement of droplets relative to the fluid. The droplet size, resulting from a dynamic equilibrium between rupture and coalescence, is broad, so there is not a predominant droplet size. Energy is supplied at large scales by a random turbulent forcing (green line) and is transferred to small scales by the work of both inertia (red line) and interfacial forces (black line). Whatever the cause of the fluctuations, interfaces turn out to be responsible for an energy transfer toward small scales.

To advance our understanding of turbulence in bubbly flows, the interaction between SIT and BIA need now to be investigated. This can be achieved by investigating the combination of the two cases illustrated in Fig. 13: a bubble swarm rising in pre-existing homogeneous isotropic turbulence (HIT). Experiments considering a bubble swarm in a grid turbulence (Alméras et al., 2017) and DNS of a bubble swarm in a forced HIT (Pandey et al., 2022) have been carried out. However, in both cases, there was not a significant overlap between the energetic scales of the BIA and the HIT, since the bubbles were rather small relative to the HIT scales. Further work should focus on a bubble size within the inertia range of HIT to pave the way to the comprehension and the modeling of more complex cases such as turbulent bubbly flows

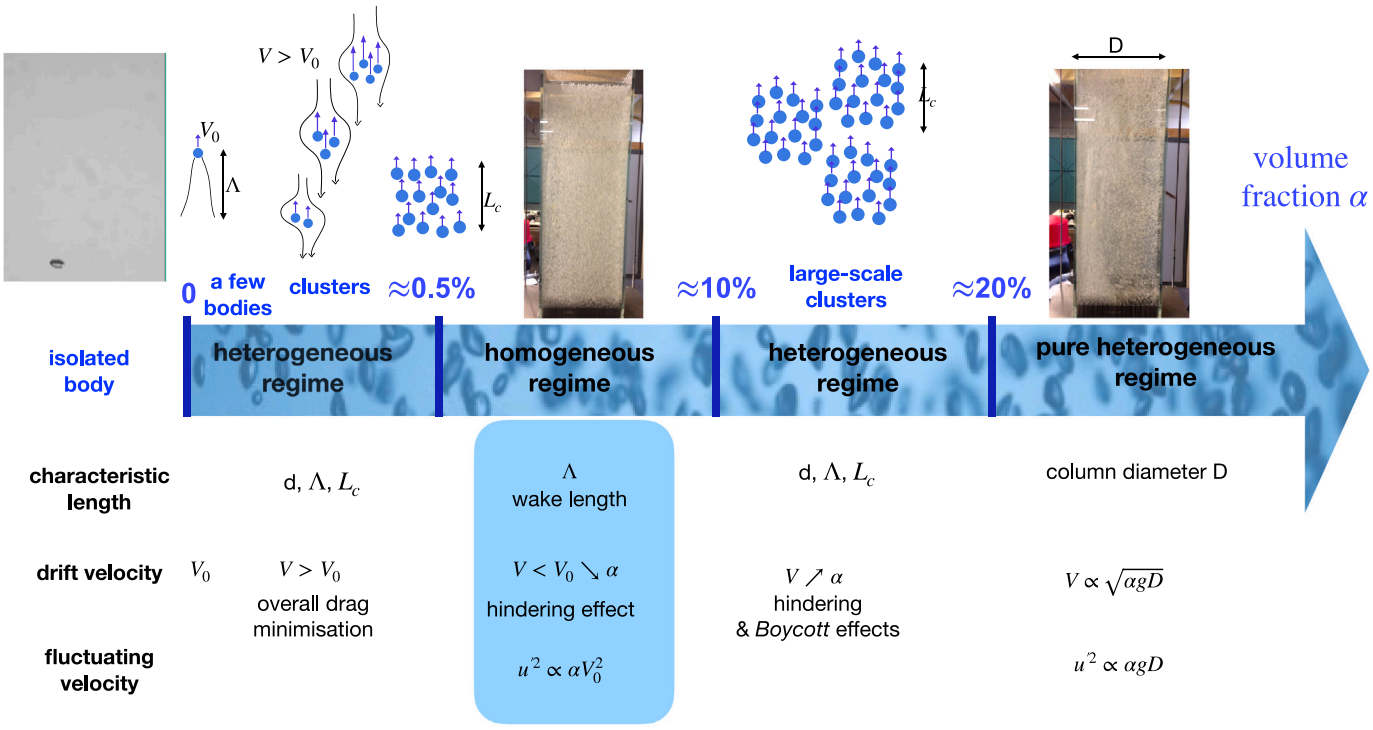

Fig. 12. Successive regimes of bubbly flows for increasing gas volume fractions.

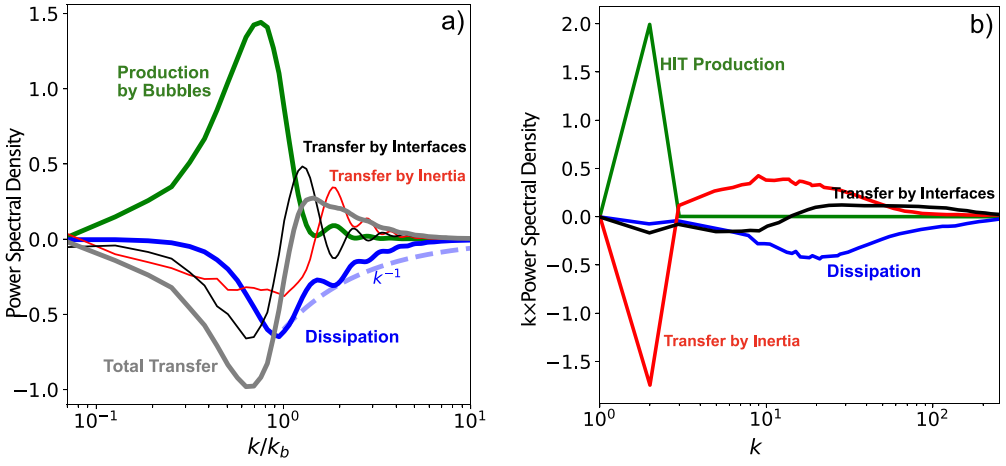

Fig. 13. Spectral Energy Budget of the two-phase mixture velocity fluctuations. (a) Monodispersed swarm of homogeneous rising bubbles at α =6% and Re=460. Adapted from Ramirez et al. (2024) with permission from Elsevier. (b) Polydispersed swarm of droplets in Homogeneous Isotropic Turbulence. Adapted from Crialesi-Esposito et al. (2022) with permission from Cambridge University Press.

in a pipe, where strong inhomogeneous turbulence produced at the wall is interacting with large bubbles (du Cluzeau et al., 2019).

The lead for Section 4.1 was taken by F.R.

4.2. Effect of bubble deformability

One of the most distinguishing features of bubbles, as compared to solid particles, is that they are deformable. Small buoyant bubbles and bubbles in very viscous fluids are generally spherical and their dynamics do not depend on surface tension. Very large buoyant bubbles are highly deformable and often appear as spherical caps and, since their drag is mainly pressure drag, their dynamics does not depend on surface tension. For bubbles of in-between sizes, surface tension matters and bubbles come is a variety of shapes, often rising unsteadily along a spiral or helical paths. Although the motion of single buoyant bubbles continues to be of interest, see Cano-Lozano et al. (2016), Hidman et al. (2022), for example, it is the impact of deformability on the collective motion of many bubbles that we will focus on here.

It has been known for a long time that the lift of a bubble in vertical shear depends strongly on the deformability of the bubble (Ervin and Tryggvason, 1997; Tomiyama et al., 2002). A single spherical bubble moving upward in vertical shear drifts laterally toward the slower moving liquid, as predicted for a solid sphere in inviscid flow (Auton, 1987), but deformation results in a reversal of the circulation around the bubble and a change in the direction of the lift. For bubble swarms the effect of deformation can be dramatic. Numerical simulations of several bubbles rising in initially quiescent flow at modest Reynolds numbers (Bunner and Tryggvason, 2002a,b, 2003; Esmaeeli and Tryggvason, 2005) showed that deformation changes the microstructure of the flow and while nearly spherical bubbles have a tendency to line up

side by side, sometimes forming horizontal "rafts", deformed bubbles have a tendency to line up, one after the other, occasionally resulting in a "streaming" instability where the bubbles rise in concentrated columns. The effect of deformability is also particularly strong for wall-bounded flows and in upflow in vertical pipes experiments (Serizawa et al., 1975; Liu and Bankoff, 1993) have shown core peaked volume fraction distribution for large bubbles and a wall peak for small bubbles. Numerical simulations of bubbly up and down flow show that it is the deformability, not size that matters. In Lu et al. (2006) the void fraction distribution in a vertical channel was examined, for both upflow and downflow, for nearly spherical bubbles. For upflow, lift pushes the bubbles to the walls, and as bubbles are removed from the channel core, the weight of the mixture increases until it balances the imposed pressure gradient. This observation, that the mixture in the middle of the channel is in hydrostatic equilibrium at a steady state, makes it possible to predict the volume fraction there and once we have determined how much air needs to be removed from the core, the volume fraction in the wall layer can be determined. For downflow, the opposite is true and lift pushes bubbles away from the walls, increasing the buoyancy in the bulk of the channel until it matches the pressure gradient pushing the flow downward. At steady state the volume fraction is therefore easily predicted analytically, as well as the thickness of the bubble-free layer near the walls. The velocity in the center is constant for both upflow and downflow and for downflow the results show that using results for single-phase parallel flows allows us to predict the flow rate analytically.

For upflow the flow in the wall layer is more complex due to the presence of bubbles, but a scaling analysis by Dabiri and Bhuvankar (2016) cast some light on its structure. For turbulent flow the flow structure is similar. For downflow, simulations of different void fractions (Lu and Tryggvason, 2006) and bubble sizes (Lu and Tryggvason, 2007) show that the simple solution for the volume fraction profile found for laminar flows holds also for turbulent flows and for downflow the flow rate can be predicted by using the law-of-wall in the bubble-free wall-layer. Simulations of more deformable bubbles in turbulent upflow (Lu and Tryggvason, 2008) confirm that the void fraction distribution is peaked near the walls for nearly spherical bubbles (and the steady state distribution can be predicted in the same way as for laminar flow), but deformable bubbles remain in the middle of the channel and result in a nearly bubble-free wall layer. For the parameters examined, the flow rate was essentially the same as for single-phase flows, once the total pressure gradient was adjusted to account for the addition of the bubbles. These simulations were for fairly small systems, but simulations with a larger number of bubbles have confirmed the results (Lu and Tryggvason, 2013; Tryggvason et al., 2016). The larger simulation showed that the bubbles in the wall layer cluster in a way seen experimentally by Takagi et al. (2008) for small bubbles that are prevented from coalescing by adding a small amount of surfactant.

Other situations where the effect of bubble deformability is critical can be found in bubble-induced drag reduction, were bubbles injected into turbulent flow only lead to drag reduction if the bubbles are deformable. The mechanism was examined by Lu et al. (2005) who showed that for the parameters they examined the drag reduction was due to deformable bubbles sliding over streamwise vortices and pushing them into the wall, where they are dissipated by wall-bounded vorticity of the opposite sign. This reduction of streamwise vorticity reduced the exchange of high and low-speed fluids and resulted in drag reduction. Spherical bubbles, on the other hand, are slowed down when they reach into the viscous wall layer and lead to a drag increase.

A very similar mechanism is at play in bubbly turbulent Taylor–Couette flow (Grossmann et al., 2016). There in clean water bubble injection with a small volume fraction of 4% leads to massive drag reduction by 40% (van Gils et al., 2013). The deformability of these bubbles plays the major role; they accumulate close to the inner boundary layer and reduce the momentum exchange between bulk and boundary layer. However, when injecting one drop of the surfactant of Triton-X into the Taylor–Couette flow, which has a volume of 111 liters, the effect of the bubble drag reduction is nearly completely gone (Verschoof et al., 2016). The reason for this is that the surfactant prevents bubble coalescence, and therefore the bubbles, which are continuously disintegrated in the strongly driven turbulence, in average become much smaller and are therefore spherical. However, spherical bubbles are much less efficient in blocking the momentum transfer between the bulk and the boundary layers; therefore, the drag is hardly reduced. The same effect is seen in direct numerical simulations (Spandan et al., 2018b) with an advanced finite difference code, coupled to an immersed boundary layer scheme for the deformable bubbles (Spandan et al., 2018a).

While many experiments and nearly all numerical simulations have focused on disperse flows where the bubbles for the most part retain their identities, in real systems coalescence and breakup usually take place. At low volume fraction those can be treated as relatively isolated events, but as the volume fraction increases the topology changes are more frequent and the interfaces convoluted. Flows where the bubbles coalesce and break apart again repeatedly have been examined in Lu and Tryggvason (2018, 2019). Topology changes in multiphase flows, where fluid blobs coalesce and breakup, in principle, require the resolution of processes that take place on a much smaller scale than then rest of the fluid (rupture of films and breaking of threads) and are therefore difficult to resolve. However, by carefully controlling the topology change at the resolved scale, it was possible to produce results that were relatively insensitive to the resolution and specific parameters controlling the topology change (at least for the situation examined). For low volume fraction, the simulations showed the emergence of preferred bubble sizes but at higher volume fractions the flow no longer could be described as disperse flows. We note that the statistical description of multiphase flows with complex interface topology is considerably more complex than for disperse flows and both papers examined various ways to do so, including by the use of various correlation functions and area projections.

The lead for Section 4.2 was taken by G.T.

5. Mass transfer in bubbly flows

For bubbles not in thermodynamic equilibrium with the surrounding liquid, transfer processes occur that are accompanied by the production of entropy at the gas/liquid (g/l) interface. Actual gas–liquid systems are composed of several chemical constituents, rather than of a vapor bubble inside a liquid phase of the same, pure component. Here, main emphasis is hence put on the multi-component case with two or more constituents, where at least one of them is transferred across the fluid interface. Relevant examples include ocean-atmospheric exchange (Deike, 2022), the capture or storage of CO_2 or chemical reactions inside bubble columns (Schlüter et al., 2021).

The overall mass transfer rate is an integral quantity that is determined as the result of a complex local interplay between the two-phase hydrodynamics, advection of the dissolved species, possibly chemical reactions and the dynamics of the bubble's surface and its surface properties, where the latter is significantly influenced by contaminants or additives that are surface active, so-called surfactants. The current understanding of transport phenomena at fluid interfaces has gained enormously from recent advances in Computational Engineering, employing direct numerical simulations (DNS), i.e. accurate numerical solutions of the governing equations that account for the above mentioned physico-chemical mechanisms and their interplay, under full resolution of all relevant time and length scales. This requires techniques for high performance computation as well as thermodynamically consistent mathematical models of high fidelity.

Mass transfer of chemical species across the surface of bubbles can be described using sharp-interface continuum thermodynamics, employing the balances of mass, momentum and species mass. In this context, detailed models are usually based on the isothermal two-phase

Navier–Stokes equations for incompressible fluids, together with jump conditions for mass and momentum. To model the local transfer of a chemical species across the interface, this system of partial differential equations is to be complemented by reaction-advection-diffusion equations, plus interfacial jump conditions, for all constituents present in the physical system. At this point, the complexity of the model severely depends on whether the system is clean or contaminated.

5.1. Mass transfer at clean bubbles

Without the presence of surface active agents, the following species jump conditions are usually employed:

$$D_i^l \nabla c_i^l \cdot \mathbf{n} = D_i^g \nabla c_i^l \cdot \mathbf{n} \quad \text{and} \quad c_i^l = c_i^g / H_i \quad \text{at } \Sigma, \tag{4}$$

where Σ is the interface with unit normal $\mathbf{n}$, $c_i^{g/l}$ and $D_i^{g/l}$ are the molar concentrations and the (Fickean) diffusivities in the gas (g) and liquid (l) phase, respectively, and $H_i > 0$ is the Henry coefficient. All model parameters are functions of temperature T and pressure p. See, e.g., Bothe and Fleckenstein (2013) for a detailed derivation of this model and the underlying assumptions.

Concerning the numerical simulation of mass transfer at bubbles, several challenges result from the species jump conditions. Due to $(4)_2$, the concentrations c_i have a jump discontinuity at the interface, which has to be treated consistently with the respective approach for the two-phase Navier–Stokes system. This has first been tackled with the geometric Volume of Fluid (VOF) method (Davidson and Rudman, 2002; Bothe et al., 2004), followed by the Front Tracking and the (extended) Level Set method (Hayashi and Tomiyama, 2011; Darmana et al., 2006; Koynov et al., 2005a), all in two-dimensional or axisymmetric settings. Later, detailed mass transfer simulations in 3D have been performed, e.g., with VOF (Onea et al., 2009; Bothe and Fleckenstein, 2013) and Level Set (Lehrenfeld and Reusken, 2012; Balcázar-Arciniega et al., 2019a). A different approach (Haroun et al., 2010; Marschall et al., 2012) uses the algebraic VOF method with governing equations which result from conditional averaging of the sharp-interface model. This has been extended further in Maes and Soulaine (2018, 2020), Zanutto et al. (2022). Often, artificially increased diffusivities D_i^l have been used, because the concentration boundary layer thickness λ_c inside the liquid phase scales as $\lambda_{\mathrm{hyd}}/\sqrt{\mathrm{Sc}_i}$, where λ_{hyd} denotes the thickness of the hydrodynamical boundary layer at the bubble surface and $\mathrm{Sc}_i = \nu / D_i^l$ is the Schmidt number for species i with ν the kinematic viscosity. With Sc of the order 10^2-10^3 for small molecules and up to 10^5 or higher for the diffusion of macromolecules in liquids, this leads to extremely thin species boundary layers (SBLs), which poses a severe resolution problem to 3D mass transfer simulations for realistic material parameters (Calmet and Magnaudet, 1998), hardly resolvable solely by adaptive grid techniques. To overcome the high Sc problem at fluid interfaces, different approaches have been proposed. In Aboulhasanzadeh et al. (2012, 2013a), the surface grid of the Front Tracking method is exploited to solve the species boundary layer equations along the fluid particle surface. This approach also extends to 3D flows, where the computational savings is even greater (Aboulhasanzadeh et al., 2013b; Aboulhasanzadeh and Tryggvason, 2014; Claassen et al., 2020). In Panda et al. (2019), adaptive refinement has been combined with a dual grid for scalar transport. Based on a local analysis of the SBL in a parabolized version, a nonlinear subgrid-scale flux reconstruction was introduced in Alke et al. (2010), which was further enhanced and assessed in Bothe and Fleckenstein (2013), Weber et al. (2017), Weiner and Bothe (2017), Weiner (2020), Weiner et al. (2022), Maarek (2024), allowing the accurate computation of SBLs fully embedded inside the interfacial grid cell. Some results from the various approaches are visualized in Fig. 14.

If mass transfer is accompanied by chemical reactions, the conversion of educts into products as well as selectivities become the result of an even more involved interplay of hydrodynamics, moving and deforming interfaces, local mass transfer and chemical reaction kinetics. Results for reactive mass transfer at bubbles, including selectivity information, have been reported in Koynov et al. (2005b), Radl et al. (2008), Falcone et al. (2018). Computations become much more challenging if the reactions are fast compared to the characteristic time for transfer across the SBL. On the one hand, the thickness of the SBL significantly decreases further. On the other hand, chemical reactions lead to stiff nonlinear terms and, usually, to a large number of species and tight coupling of the species equations. In this case, the approach via subgrid-scale modeling requires further developments. In Gründing et al. (2016), the local analytical solution is replaced by the numerical solution of a substitute problem, locally in each interface cell. Comparison between experimental and numerical mass transfer for a single chemical reaction showed good agreement (Weiner et al., 2019b). A more flexible approach has been introduced in Weiner et al. (2019a), Weiner (2020), where machine learning techniques have been employed to approximate the true face fluxes with neighboring velocity and species concentrations as input parameters. The right panel in Fig. 15 shows the complex concentration patterns resulting from purely physical mass transfer (physisorption) and from reactive transfer for a single reaction of type $A + B \rightarrow P$ between the transfer species A and a dissolved one (chemisorption), respectively. In particular, it shows the significant sharpening of the concentration boundary layer due to consumption of the transfer species by the chemical reaction. The bubble is simulated with the Volume of Fluid method until quasi-steady rise, using Basilisk (Popinet, 2014). Having the bubble shape and the flow field, a body-fitted mesh is generated and the single-phase Navier–Stokes equations with Dirichlet data for the velocity are solved together with species equations, where the cell-local mass transfer is computed using a data-driven subgrid-scale flux correction; see Weiner et al. (2019a), Weiner (2020) for details.

Species transfer leads to volume changes, which can become intense for high solubilities (i.e., small values of H_i) or for fast consumption of the transfer species during chemical reaction. To account for such local volume effects, the first species jump condition $(4)_1$ needs to be replaced by the following, more general form:

$$\left(c_i^l(\mathbf{v} - \mathbf{v}^\Sigma) - D_i^l \nabla c_i^l\right) \cdot \mathbf{n} = \left(c_i^g(\mathbf{v} - \mathbf{v}^\Sigma) - D_i^g \nabla c_i^l\right) \cdot \mathbf{n} \quad \text{at } \Sigma. \tag{5}$$

Note that (5) allows for a relative (normal) motion of the interface against the bulk phases induced by mass transfer, similarly to phase change jump conditions. While global volume effects have already been accounted for in Hayashi and Tomiyama (2011) with a front tracking method, such local volume effects have been computed with the geometric VOF method in Fleckenstein and Bothe (2015) and with the algebraic VOF method in Maes and Soulaine (2020). Note that the basic VOF phase indicator transport equation $\partial_t \chi + \mathbf{v} \cdot \nabla \chi = 0$ needs to be extended considerably as there is a volume source/sink at the interface (Fleckenstein and Bothe, 2015). The left panel in Fig. 15 displays snapshots from 3D Volume of Fluid simulation of the dissolution process for a CO_2 Taylor bubble placed in a 70 vol% glycerol/water mixture, where the liquid flows from right to left around the bubble.

5.2. Mass transfer at contaminated bubbles

Surface active agents, so-called surfactants, are of crucial relevance in a great variety of applications and their importance for multiphase processes can hardly be overestimated. Changing the interfacial tension in dependence on the local surface concentration of adsorbed surfactant induces Marangoni stresses, which alter the local flow field, possibly damping or, to the contrary, destabilizing the fluid particle. This has a significant effect on the fluid particle shape, hence on the interfacial area and rise velocity, on the global residence time of fluid particles, the local residence time of chemical species near the interface, the appearance or structure of a wake, the coalescence and breakup behavior, and ultimately on the characteristics of the drop or bubble population (Takagi and Matsumoto, 2011). These effects are

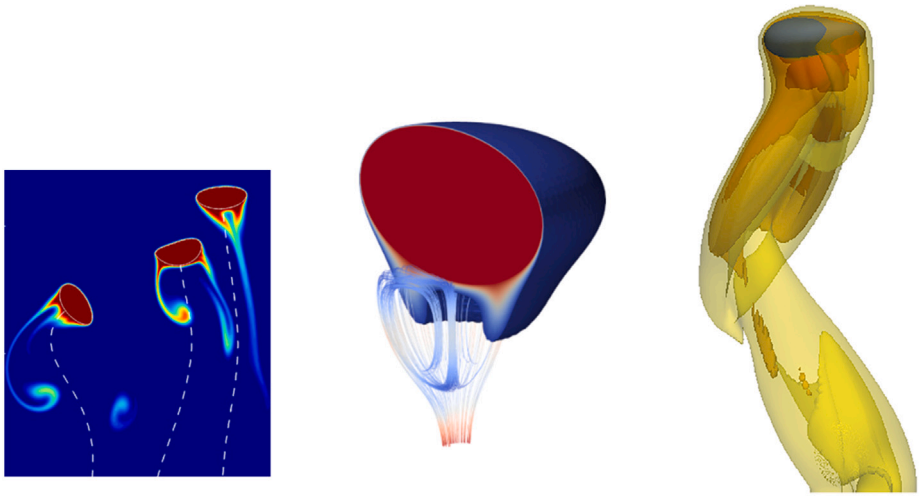

Fig. 14. Results from mass transfer computations using subgrid-scale modeling. Left: Concentration field around a group of three freely rising bubbles in 2D (Re=60, Sc=13, t=12.3), obtained by Front Tracking simulations with species equation plus additional boundary layer transport equations applied along the bubble surface (part of Fig. 8 in Aboulhasanzadeh et al. (2012), reproduced with permission from Elsevier). Middle: Concentration field around a freely rising bubble in 3D (Re=60, Sc=500, log(Mo)=-5), obtained by ALE Interface Tracking simulations in Weber et al. (2017), employing the subgrid-scale modeling developed in Bothe and Fleckenstein (2013). Reproduced with permission from Elsevier. Right: Concentration field for a wobbling bubble rising freely in 3D (Re=977, Sc=920, log(Mo)=-11). Simulation using Front Tracking with species equation plus additional boundary layer transport equations, building on and further extending the approach from (Aboulhasanzadeh et al., 2012) (part of Fig. 6 in Claassen et al. (2020), reproduced with permission from John Wiley and Sons).

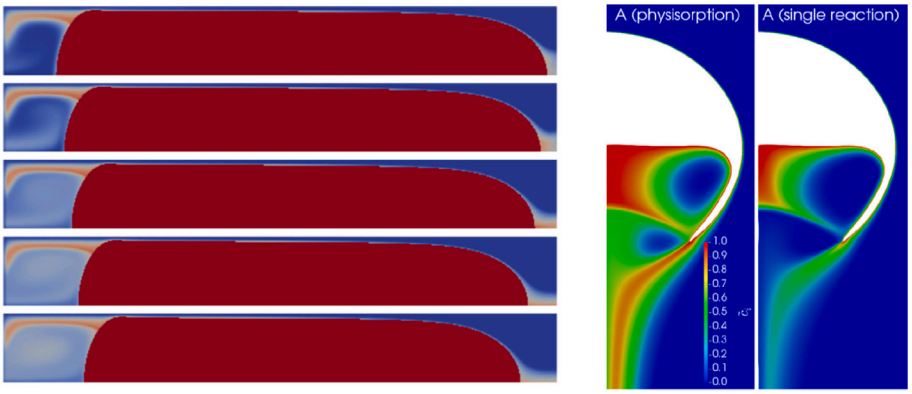

Fig. 15. Left: Cross sections of a dissolving CO_2 Taylor bubble in 70 vol% glycerol/water mixture, computed with an extended 3D Volume of Fluid method (Fig. 9 in Fleckenstein and Bothe (2015), reproduced with permission from Elsevier). Mass transfer computation started after the flow field is developed. Snapshots of the CO_2 concentration at time $t = 0.01$ s, 0.03 s, 0.05 s, 0.07 s and 0.09 s (top to bottom). Right: Concentration fields around a freely rising dimpled ellipsoidal bubble for physisorption and chemisorption (rightmost picture) with a single reaction of type $A + B \rightarrow P$ (Re= 8.4, Sc=5800, log(Mo)=1.51, Da = 0.3; part of Figure 71 in Weiner (2020).

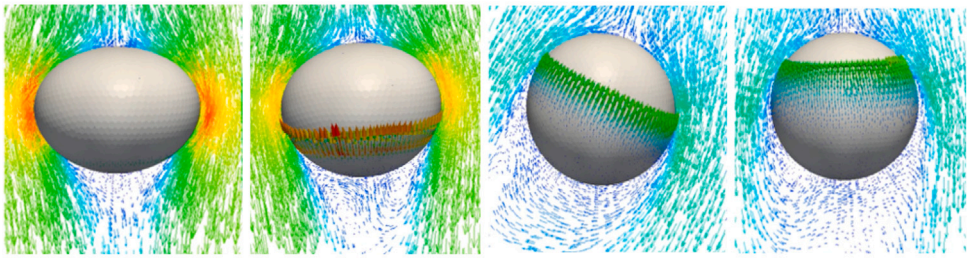

Fig. 16. Results from an ALE Interface Tracking simulation of an air bubble, initially of spherical shape with diameter of 1.45 mm, rising in an aqueous surfactant solution. The initial surfactant concentrations in the liquid phase corresponds to a Marangoni number of Ma=34. The pictures show bulk velocity vectors and interfacial Marangoni forces at different time instances (colored by magnitude). Snapshots are from the simulation reported in Pesci et al. (2018), cf. Fig. 25 there. Reproduced with permission from Cambridge University Press.

rarely quasi-stationary but transient and highly nonlinear, inducing for instance a non-monotonic (in time) rise behavior; see Pesci et al. (2018) and the references given there.

Simulating fluid particles with surfactant adsorbed to their interface requires the numerical solution of partial differential equations on moving and deforming surfaces with a strong influence of the local curvature. In the case of soluble surfactant – a common case in applications – the nonlinear coupling between bulk and interfacial surfactant concentrations needs to be included in a mass conservative way. First developments of numerical methods (Tryggvason et al., 1992; James

and Lowengrub, 2004; Lee and Pozrikidis, 2006; Xu et al., 2006) have therefore been restricted to 2D or axisymmetric flows and to insoluble surfactants. Numerical method for soluble surfactant have been developed based on the Front Tracking method (Muradoglu and Tryggvason, 2008, 2014; de Jesus et al., 2015), the geometric VOF method (Alke and Bothe, 2009), the ALE Interface Tracking method (Dieter-Kissling et al., 2015; Pesci et al., 2018) based on (Tuković and Jasak, 2012), as well as the Level Set Method (Ganesan and Tobiska, 2012; Xu et al., 2012; de Langavant et al., 2017; Shin et al., 2018). All results discussed above for soluble surfactants used artificially increased diffusivities of the surfactant. To capture the non-monotonic rise velocity behavior of an initially clean bubble rising in a surfactant solution, a realistic (small) diffusivity of the surfactant species is required. Combining the subgrid-scale flux reconstruction from (Weiner and Bothe, 2017) with the interface tracking surfactant method from (Dieter-Kissling et al., 2015), the correct rise dynamics has been obtained in Pesci et al. (2018). Fig. 16 displays representative snapshots during the rise of an initially spherical and clean bubble through an aqueous surfactant solution. The bubble immediately deforms during its acceleration and starts accumulating surfactant, with bulk-surface sorption modeled by the Langmuir isotherm. Due to tangential advection along the interface, the surfactant is inhomogeneously distributed on the bubble surface. Consequently, Marangoni stress builds up, slowing down the bubble and bringing it back to an almost spherical shape. The initial surfactant concentrations in the liquid phase corresponds to a Marangoni number of Ma=34. In this regime, the bubble velocity goes through a maximum before the bubble decelerates until reaching a quasi-steady terminal velocity being close to the one for high surfactant concentrations. The pictures in Fig. 16 show bulk velocity vectors and interfacial Marangoni forces at different time instances. The surface coverage grows during the rise, resulting in increasing Marangoni stresses. The line, where the flow detaches, corresponds to the region where the Marangoni forces are the highest. While the bubble is rising, this region moves towards the upper pole. This complex behavior results from the interplay of processes acting on different time scales, all of which need to be captured accurately for a sound description. The transport of surfactant to the interface is strongly diffusion-limited. Employing the subgrid-scale approach from (Weber et al., 2017) allows to compute this accurately, thus capturing the non-monotonic rise behavior.

Evidently, mass transfer during the motion of a fluid particle like in Fig. 16 is a complex transient process. Furthermore, surfactants with their strong influence on surface tension have tremendous effects on the local mass transfer rates at fluid interfaces, as confirmed in experimental studies (Hebrard et al., 2009; Haghnegahdar et al., 2016); see also (Nekoeian et al., 2019). While first ideas and basic models such as rise velocity correlations, aspect ratio, stagnant cap etc. are available, a precise quantitative understanding of the local interplay of all involved sub-processes and mechanisms requires detailed numerical investigation. To this end, first computational studies of mass transfer at bubbles influenced by surfactant haven been reported recently (Kentheswaran et al., 2022, 2023) and revealed interesting findings, e.g. on changes in the local Sherwood number and the importance of the (relative) tangential interface velocity.

The coverage of a fluid interface by a surfactant also partially blocks the interface, causing a hindrance effect, which is a phenomenon also relevant for evaporation processes and is additional to the Marangoni effect. First approaches for a correlation-based global model of mass transfer hindrance have been given in Sardeing et al. (2006), Hebrard et al. (2009). Recently, a thermodynamically consistent model of the local phenomenon has been derived in Bothe (2022). The crucial point there is to account for area-specific surface concentrations not only for surfactants but for all transfer species as they need to cross the interface zone while transferring from one phase to the other, hence are also present inside the transition zone. This introduces surface chemical potentials into the model and allows to account for the surface tension as a relevant surface thermodynamical state variable. The latter alters the surface chemical potentials under the influence of adsorbed surfactant, changing the mass transfer driving forces. This yields a description of the apparent blockage of the interface, being consistent to the phenomenological energy barrier model due to Langmuir; see Bothe (2022) for more details. The situation becomes even more complicated, if the liquid phase contains additional constituents such as ionic species, i.e. electrolytes, or alcohols (Aoki et al., 2017; Hori et al., 2019, 2020), as they interact with the sorption processes. A detailed computational study of mass transfer at bubbles or, more generally, at fluid interfaces for such complex multi-component liquids, possibly of non-Newtonian rheology, is a rich field for future studies.

5.3. Mass transfer, reactions, and surfactants in swarms

Industrial bubble columns usually include a large number of interacting bubbles and since the dynamics of interacting bubbles is different from an isolated one the effect on mass transfer and reactions is of considerable interest. Relatively little is known, however, about what happens in swarms. Experiments (Colombet et al., 2011, 2015) and numerical simulations (Aboulhasanzadeh and Tryggvason, 2014) (for a Schmidt number equal to 100), suggest that mass transfer in swarms is comparable to that of a single bubble. This conclusion is also supported by other simulations (Roghair et al., 2016; Jin and Schlüter, 2019; Balcázar-Arciniega et al., 2019b) who generally find only a slight increase in the Sherwood number with volume fraction, particularly at higher Schmidt numbers. Fig. 17 shows one frame from a simulation of the mass transfer from a bubble swarm, using a subgrid model to account for the thin mass boundary layer (Aboulhasanzadeh and Tryggvason, 2014).

In many bubble columns the gas diffusion from the bubbles reacts with species already dissolved in the liquid and exactly what reactions take place depends on the local concentrations and mixing. While understanding the exact mechanisms determining the selectivity is of obvious interest and several authors have conducted simulations using model equations (either Euler–Euler or Euler–Lagrange), very few detailed experimental or computational studies of the dynamics at the level of a few bubbles are available. Mass transfer and reactions were examined in Koynov et al. (2005b) and the authors of Radl et al. (2008) examine the selectivity for hydrogenation of nitroarenes which can result in undesirable accumulation of hydroxylamine. Although only done for 2D flows, those studies showed that freely interacting bubbles can affect the selectivity in reacting flows, where gas diffusing from the bubbles reacts with a species dissolved in the liquid.

While we know of no numerical simulations of reacting bubble swarms in the presence of surfactants, soluble or insoluble surfactant can significantly affect the structure of bubbly flows. In Lu et al. (2017), who looked at the effect of insoluble surfactant on the dynamics of many bubbles in vertical channels, it was shown that since insoluble surfactant reduces the lift and thus the migration of bubbles to the walls, the void fraction distribution for nearly spherical bubbles in vertical channels is changed significantly, reducing or preventing the formation of wall layers. Simulations of a single bubble and soluble surfactants show the same changes in the lift (Ahmed et al., 2020b) and subsequent simulations of many bubbles have shown that soluble surfactants result in a similar volume fraction distribution as seen for insoluble surfactants (Ahmed et al., 2020a).

The lead for Section 5 was taken by D.B. and G.T.

6. Outlook

As said already in the introduction, a review on the broad subject of bubbles and bubbly flows can only discuss selected subjects; they reflect our passions and current research questions we are obsessed with. The aim of the article was to share our excitement on bubbles and bubbly flows with the reader; for more details we have referred to the original articles and more focused review articles.

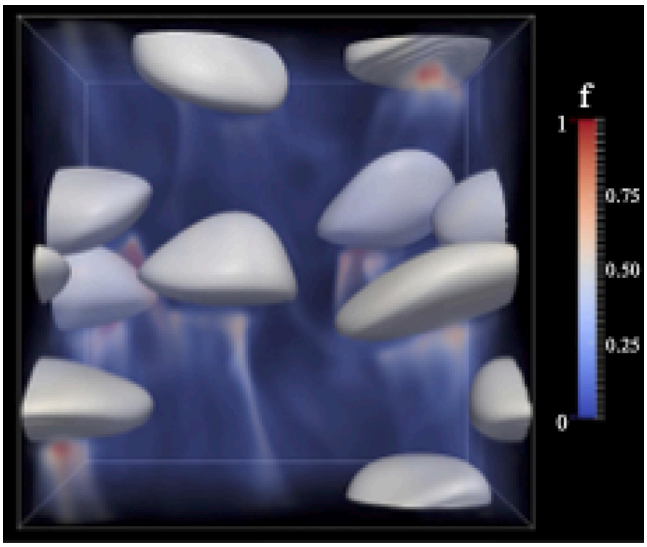

Fig. 17. Eight freely moving bubbles in a periodic domain and the distribution of scaled dissolved mass in the liquid, at one time. Here, volume fraction = 9.0%, log $Mo = -6.5$, and $Eo = 5.0$. Reproduced from (Lu et al., 2017) with permission from Elsevier.

We want to end with an outlook on future research questions and opportunities which we see for the research on bubbles and bubbly flows. It is written in the same spirit as the introduction and the whole paper: We again had to be selective and the choices reflect our own preferences, views, and interests.

But for at least two subjects there will be broad consensus on its relevance and on its promising perspectives, namely the subject of dense bubble flows, which is omnipresent in the process technology. Here fast X-ray technologies for well-resolved 3D visualization have developed tremendously over the last years (Aliseda and Heindel, 2021) so that soon a one-to-one comparison with direct numerical simulations is within reach, at least for simple geometries and not too large systems, given that also the direct numerical simulations continue to develop, due to better algorithms, parallelization, GPUs, and faster and more computational power. In this context we also mention the other subject on which there will be consensus that it will play an important role in the research on bubbly flow, namely, machine learning, as this will be the case in nearly all subfields of fluid dynamics. For further reading we refer to the two recent review articles of Brunton et al. (2020) and Kochkov et al. (2021). We are convinced that machine learning schemes which take notice of the underlying dynamical equations will be superior compared to simple data-driven machine learning algorithms.

From our point of view one of the most exciting areas for new developments and major breakthroughs is multicomponent multiphase flow with phase transitions. In Section 2 we have already discussed boiling, but mainly focusing on boiling in pure liquids. In boiling multicomponent liquids, selective evaporation leads to gradients in surface tension and thus solutal Marangoni flows. We have analyzed one peculiar example in Zeng et al. (2021), where we observed and analyzed periodic bouncing of a plasmonic bubble in a binary liquid by competing solutal and thermal Marangoni forces. We emphasize that in most applications the liquids are indeed of multicomponent character, and therefore such studies of boiling in multicomponent multiphase liquids are of huge relevance. We emphasize that even better numerical methods to efficiently and accurately simulate bubbly flows with heat and mass transfer in complex geometries will be needed and so are numerical methods to efficiently and accurately simulate three phase systems with additional particles as solid phase. These might be catalytic particles, which then strongly influence chemical reactions, which in turn have a strong effect on the mass transfer.

Bubbly flows which also can be viewed as being in the category of multi-component multiphase flows with phase transitions are flows with chemical reactions at the bubble-liquid interfaces or the flows which emerge in electrolysis with strong currents (the relevant case for applications!), when bubble nucleation and growth become unavoidable. Here, besides the presence of ionic species, induced electrical forces acting on the bubble are present. Moreover, also wetting plays a prominent role and interferes with the mass transfer process as transfer is expected to be different close to the contact line. Flows in which catalytic reactions with involved gas formation occur are also of multicomponent multiphase character, with phase transition.

The final flow in this category we want to mention is the freezing of multicomponent bubbly flows, as it occurs for example in the food industry. When a freezing front goes through a bubbly liquid, gas is expelled at the solid–liquid interface (Carte, 1961), as solids in general can take up less gas than liquids. The gas expulsion leads to bubble growth at the interface and for fast enough freezing rates these bubbles are finally enclosed by the freezing liquid. This mechanism leads to the opaqueness of ice blocks from frozen tap water. One of us (DL), together with his colleagues, has recently started to explore this phenomenon from a fluid dynamics point of view (Meijer et al., 2024), finding fascinating bubble growth behavior at the solid–liquid interface. In the next years we expect to see many more experiments and numerical simulations in this new and fascinating subfield of bubbles and bubbly flows.

The lead in writing this final section was taken by D.L.

Declaration of competing interest

The authors declare that they have no known competing financial interests or personal relationships that could have appeared to influence the work reported in this paper.

Acknowledgments

We thank Professor Andrea Prosperetti for all that we learnt from him on bubbles and bubbly flows (and beyond) in the last 30+ years and for his leadership in the field. We take the opportunity to congratulate him on his upcoming 80th birthday! We also thank him for his long-term leadership as Editor-in-Chief of the International Journal of Multiphase Flow.

Data availability

No data was used for the research described in the article.

References

Aboulhasanzadeh, B., Hosoda, S., Tomiyama, A., Tryggvason, G., 2013a. A validation of an embedded analytical description approach for the computations of high Schmidt number mass transfer from bubbles in liquids. Chem. Eng. Sci. 101, 165–174.

Aboulhasanzadeh, B., Hosoda, S., Tomiyama, A., Tryggvason, G., 2013b. A validation of an embedded analytical description approach to the computations of mass transfer from bubbles in high Schmidt number liquids. Chem. Eng. Sci. 101, 165–174.

Aboulhasanzadeh, B., Thomas, S., Taeibi-Rahni, M., Tryggvason, G., 2012. Multiscale computations of mass transfer from buoyant bubbles. Chem. Eng. Sci. 75, 456–467.

Aboulhasanzadeh, B., Tryggvason, G., 2014. Effect of bubble interactions on mass transfer in bubbly flow. Int. J. Heat Mass Transfer 79, 390–396.

Abrams, C., Bussi, G., 2014. Enhanced sampling in molecular dynamics using metadynamics, replica-exchange, and temperature-acceleration. Entropy 16, 163–199.

Adhikari, U., Goliaei, A., Berkowitz, M.L., 2016. Nanobubbles, cavitation, shock waves and traumatic brain injury. Phys. Chem. Chem. Phys. 18 (48), 32638–32652.

Ahmed, Z., Izbassarov, D., Costa, P., Muradoglu, M., Tammisola, O., 2020a. Turbulent bubbly channel flows: Effects of soluble surfactant and viscoelasticity. Comput. Fluids 212, 104717.

Ahmed, Z., Izbassarov, D., Tryggvason, G., Muradoglu, M., Tammisol, O., 2020b. Effects of soluble surfactant on lateral migration of a bubble in a pressure driven channel flow. Int. J. Multiph. Flow 126, 12, 103251.
Aliseda, A., Heindel, T.J., 2021. X-ray flow visualization in multiphase flows. Annu. Rev. Fluid Mech. 53 (1), 543–567.
Alke, A., Bothe, D., 2009. 3D numerical modeling of soluble surfactant at fluidic interfaces based on the Volume-of-Fluid method. Fluid Dyn. Mater. Process. 1 (1–29), 182.
Alke, A., Bothe, D., Kröger, M., Weigand, B., Weirich, D., Weking, H., 2010. Direct numerical simulation of high Schmidt number mass transfer from air bubbles rising in liquids using the Volume-of-Fluid method. Ercoftac Bull. 82, 5–10.
Allen, J.S., Roy, R.A., 2000. Dynamics of gas bubbles in viscoelastic fluids. II. Nonlinear viscoelasticity. J. Acoust. Soc. Am. 108 (4), 1640–1650.
Allred, T.P., Weibel, J.A., Garimella, S.V., 2021. The role of dynamic wetting behavior during bubble growth and departure from a solid surface. Int. J. Heat Mass Transfer 172, 121167.
Alméras, E., Masbernat, O., Risso, F., Fox, R.O., 2019. Fluctuations in inertial dense homogeneous suspensions. Phys. Rev. Fluids 4, 102301.
Alméras, E., Mathai, V., Lohse, D., Toschi, F., 2017. Experimental investigation of the turbulence induced by a bubble swarm rising within incident turbulence. J. Fluid Mech. 825, 1091–1112.
Alméras, E., Risso, F., Masbernat, O., Fox, R.O., 2021. Statistics of velocity fluctuations in a homogeneous liquid fluidized bed. Phys. Rev. Fluids 6, 034301.
Amidu, M.A., Addad, Y., Riahi, M., 2020. A hybrid multiphase flow model for the prediction of both low and high void fraction nucleate boiling regimes. Appl. Therm. Eng. 178, 115625.
Amin, A., Girolami, L., Risso, F., 2021. On the fluidization/sedimentation velocity of a homogeneous suspension in a low-inertia fluid. Powder Technol. 391, 1–10.
Amoura, Z., Besnaci, C., Risso, F., Roig, V., 2017. Velocity fluctuations generated by the flow through a random array of spheres: a model of bubble-induced agitation. J. Fluid Mech. 823, 592–616.
Aoki, J., Hori, Y., Hayashi, K., Hosokawa, S., Tomiyama, A., 2017. Mass transfer from single carbon dioxide bubbles in alcohol aqueous solutions in vertical pipes. Int. J. Heat Mass Transfer 108, 1991–2001.
Ardo, S., Rivas, D.F., Modestino, M.A., Greiving, V.S., Abdi, F.F., Llado, E.A., Artero, V., Ayers, K., Battaglia, C., Becker, J.-P., et al., 2018. Pathways to electrochemical solar-hydrogen technologies. Energy & Environ. Sci. 11 (10), 2768–2783.
Astarita, G., Apuzzo, G., 1965. Motion of gas bubbles in non-Newtonian liquids. AIChE J. 11 (5), 815–820.
Atchley, A.A., Prosperetti, A., 1989. The crevice model of bubble nucleation. J. Acoust. Soc. Am. 86 (3), 1065–1084.
Auton, T., 1987. The lift force on a spherical body in a rotational flow. J. Fluid Mech. 183, 190–218.
Azouzi, M.E.M., Ramboz, C., Lenain, J.-F., Caupin, F., 2013. A coherent picture of water at extreme negative pressure. Nat. Phys. 9 (1), 38–41.
Badillo, A., 2012. Quantitative phase-field modeling for boiling phenomena. Phys. Rev. E - Stat. Nonlinear, Soft Matter Phys. 86.
Balachandar, S., Eaton, J.K., 1984. Turbulent dispersed multiphase flow. Annu. Rev. Fluid Vol. 43 42, 111–133.
Balcázar-Arciniega, N., Antepara, O., Rigola, J., Oliva, A., 2019a. A level-set model for mass transfer in bubbly flows. Int. J. Heat Mass Transfer 138, 335–356.
Balcázar-Arciniega, N., Antepara, O., Rigola, J., Oliva, A., 2019b. A level-set model for mass transfer in bubbly flows. Int. J. Heat Mass Transfer 138, 335–356.
Bao, B., Zandavi, S.H., Li, H., Zhong, J., Jatukaran, A., Mostowfi, F., Sinton, D., 2017. Bubble nucleation and growth in nanochannels. Phys. Chem. Chem. Phys. 19, 8223–8229.
Bartell, L.S., 2001. Nucleation of vapor bubbles in water: Experiment and theory. J. Phys. Chem. B.
Batchelor, D.V., Armistead, F.J., Ingram, N., Peyman, S.A., Mclaughlan, J.R., Coletta, P.L., Evans, S.D., 2021. Nanobubbles for therapeutic delivery: Production, stability and current prospects. Curr. Opin. Colloid Interface Sci. 54.
Blander, M., Katz, J.L., 1975. Bubble nucleation in liquids. AIChE J. 21 (5), 833–848.
Bokman, G.T., Supponen, O., Mäkiharju, S.A., 2022. Cavitation bubble dynamics in a shear-thickening fluid. Phys. Rev. Fluids 7, 023302.
Bonnefis, P., Fabre, D., Magnaudet, J., 2023. When, how, and why the path of an air bubble rising in pure water becomes unstable. Proc. Natl. Acad. Sci. 120 (11), e2300897120.
Bonnefis, P., Sierra-Ausin, J., Fabre, D., Magnaudet, J., 2024. Path instability of deformable bubbles rising in Newtonian liquids: A linear study. J. Fluid Mech. 980, A19.
Borden, M.A., Song, K.-H., 2018. Reverse engineering the ultrasound contrast agent. Adv. Colloid Interface Sci..
Bothe, D., 2022. Sharp-interface continuum thermodynamics of multicomponent fluid systems with interfacial mass. Internat. J. Engrg. Sci. 179, e103731.
Bothe, D., Fleckenstein, S., 2013. Modeling and VOF-based numerical simulation of mass transfer processes at fluidic particles. Chem. Eng. Sci. 101, 283–302.
Bothe, D., Koebe, M., Wielage, K., Prüss, J., Warnecke, H.-J., 2004. Direct numerical simulation of mass transfer between rising gas bubbles and water. Bubbly Flows: Anal. Model. Calc. 159–174.
Bothe, D., Niethammer, M., Pilz, C., Brenn, G., 2022. On the molecular mechanism behind the bubble rise velocity jump discontinuity in viscoelastic liquids. J. Non-Newton. Fluid Mech. 302, 104748.
Bouche, E., Roig, V., Risso, F., Billet, A.-M., 2014. Homogeneous swarm of high-Reynolds-number bubbles rising within a thin gap. Part 2. Liquid dynamics. J. Fluid Mech. 758, 508–521.
Bourdon, B., Bertrand, E., Di Marco, P., Marengo, M., Rioboo, R., Coninck, J.D., 2015. Wettability influence on the onset temperature of pool boiling: Experimental evidence onto ultra-smooth surfaces. Adv. Colloid Interface Sci. 221, 34–40.
Bourdon, B., Rioboo, R., Marengo, M., Gosselin, E., Coninck, J.D., 2012. Influence of the wettability on the boiling onset. Langmuir 28, 1618–1624.
Bouwhuis, W., van der Veen, R.C.A., Tran, T., Keij, D.L., Winkels, K.G., Peters, I.R., van der Meer, D., Sun, C., Snoeijer, J.H., Lohse, D., 2012. Maximal air bubble entrainment at liquid-drop impact. Phys. Rev. Lett. 109, 264501.
Brenner, M.P., Hilgenfeldt, S., Lohse, D., 2002. Single bubble sonoluminescence. Rev. Modern Phys. 74, 425–484.
Brunton, S.L., Noack, B.R., Koumoutsakos, P., 2020. Machine learning for fluid mechanics. Annu. Rev. Fluid Mech. 52 (1), 477–508.
Bunner, B., Tryggvason, G., 2002a. Dynamics of homogeneous bubbly flows: Part 1. Rise velocity and microstructure of the bubbles. J. Fluid Mech. 466, 17–52.
Bunner, B., Tryggvason, G., 2002b. Dynamics of homogeneous bubbly flows. Part 2, fluctuations of the bubbles and the liquid. J. Fluid Mech. 466, 53–84.
Bunner, B., Tryggvason, G., 2003. Effect of bubble deformation on the stability and properties of bubbly flows. J. Fluid Mech. 495, 77–118.
Bures, L., Sato, Y., 2021. On the modelling of the transition between contact-line and microlayer evaporation regimes in nucleate boiling. J. Fluid Mech. 916, A53.
Bures, L., Sato, Y., 2022. Comprehensive simulations of boiling with a resolved microlayer: validation and sensitivity study. J. Fluid Mech. 933, A54.
Calmet, I., Magnaudet, J., 1998. High-Schmidt number mass transfer through turbulent gas-liquid interfaces. Int. J. Heat Fluid Flow 19 (5), 522–532.
Cano-Lozano, J.C., Martínez-Bazán, C., Magnaudet, J., Tchoufag, J., 2016. Paths and wakes of deformable nearly spheroidal rising bubbles close to the transition to path instability. Phys. Rev. Fluids 1, 053604.
Carey, V.P., 2018. Liquid-Vapor Phase-Change Phenomena: An Introduction to the Thermophysics of Vaporization and Condensation Processes in Heat Transfer Equipment, second ed. CRC Press.
Carte, A., 1961. Air bubbles in ice. Proc. Phys. Soc. 77 (3), 757.
Cavicchi, R.E., Avedisian, C.T., 2007. Bubble nucleation and growth anomaly for a hydrophilic microheater attributed to metastable nanobubbles. Phys. Rev. Lett. 98.
Chang, Y.H., Ferng, Y.M., 2019. Experimental investigation on bubble dynamics and boiling heat transfer for saturated pool boiling and comparison data with previous works. Appl. Therm. Eng. 154, 284–293.
Chatenet, M., Pollet, B.G., Dekel, D.R., Dionigi, F., Deseure, J., Millet, P., Braatz, R.D., Bazant, M.Z., Eikerling, M., Staffell, I., et al., 2022. Water electrolysis: from textbook knowledge to the latest scientific strategies and industrial developments. Chem. Soc. Rev. 51 (11), 4583–4762.
Chen, Y.-J., Ling, K., Ding, H., Wang, Y., Jin, S.-Q., Tao, W.-Q., 2022. 3-D numerical study of subcooled flow boiling in a horizontal rectangular mini-channel by VOSET. Int. J. Heat Mass Transfer 183, 122218.
Chen, Y., Yu, B., Lu, W., Wang, B., Sun, D., Jiao, K., Zhang, W., Tao, W., 2024. Review on numerical simulation of boiling heat transfer from atomistic to mesoscopic and macroscopic scales. Int. J. Heat Mass Transfer 225.
Choi, J.J., Selert, K., Vlachos, F., Wong, A., Konofagou, E.E., 2011. Noninvasive and localized neuronal delivery using short ultrasonic pulses and microbubbles. Proc. Natl. Acad. Sci. 108 (40), 16539–16544.
Church, C.C., 1995. The effects of an elastic solid surface layer on the radial pulsations of gas bubbles. J. Acoust. Soc. Am. 97, 1510–1521.
Claassen, C., Islam, S., Peters, E., Deen, N., Kuipers, J., Baltussen, M., 2020. An improved subgrid scale model for front-tracking based simulations of mass transfer from bubbles. AIChE J. 66 (4), e16889.
du Cluzeau, A., Bois, G., Toutant, A., 2019. Analysis and modelling of Reynolds stresses in turbulent bubbly up-flows from direct numerical simulations. J. Fluid Mech. 866, 132–168.
Col, D.D., Colin, C., Iorio, C., Marengo, M., Stephan, P., Tadrist, L., Di Marco, P., 2021. Physical sciences – Two-phase heat and mass transfer. ESA SciSpace Res. White Pap..
Collier, J.G., Thome, J.R., 1994. Convective Boiling and condensation, third ed. Oxford University Press.
Colombet, D., Legendre, D., Cockx, A., Risso, F., Daniel, C., Galinat, S., 2011. Experimental study of mass transfer in a dense bubble swarm. Chem. Eng. Sci. 66, 3432–3440.
Colombet, D., Legendre, D., Frédéric, Cockx, R.A., Guiraud, P., 2015. Dynamics and mass transfer of rising bubbles in a homogenous swarm at large gas volume fraction. J. Fluid Mech. 763, 254–285.
Colombo, M., Fairweather, M., 2015. Prediction of bubble departure in forced convection boiling: A mechanistic model. Int. J. Heat Mass Transfer 85, 135–146.
Cooper, M.G., Lloyd, A.J.P., 1969. The microlayer in nucleate pool boiling. Int. J. Heat Fluid Flow 12, 895–913.
Coussios, C.C., Roy, R.A., 2008. Applications of acoustics and cavitation to noninvasive therapy and drug delivery. Annu. Rev. Fluid Mech. 40, 395–420.

Crialesi-Esposito, M., Rosti, M.E., Chibbaro, S., Brandt, L., 2022. Modulation of homogeneous and isotropic turbulence in emulsions. J. Fluid Mech. 940, A19.
Dabiri, S., Bhuvankar, P., 2016. Scaling law for bubbles rising near vertical walls. Phys. Fluids 28, 062101.
Darmana, D., Deen, N., Kuipers, J., 2006. Detailed 3D modeling of mass transfer processes in two-phase flows with dynamic interfaces. Chem. Eng. Technol. 29 (9), 1027–1033.
Davidson, M., Rudman, M., 2002. Volume-of-fluid calculation of heat or mass transfer across deforming interfaces in two-fluid flow. Numer. Heat Transf.: Part B: Fundam. 41 (3–4), 291–308.
De Corato, M., Saint-Michel, B., Makrigiorgos, G., Dimakopoulos, Y., Tsamopoulos, J., Garbin, V., 2019. Oscillations of small bubbles and medium yielding in elastoviscoplastic fluids. Phys. Rev. Fluids 4, 073301.
De Groot, S.R., Mazur, P., 2013. Non-Equilibrium Thermodynamics. Courier Corporation.
de Jesus, W., Roma, A., Pivello, M., Villar, M., da Silveira-Neto, A., 2015. A 3D front-tracking approach for simulation of a two-phase fluid with insoluble surfactant. J. Comput. Phys. 281, 403–420.
de Langavant, C., Guittet, A., Theillard, M., Temprano-Coleto, F., Gibou, F., 2017. Level-set simulations of soluble surfactant driven flows. J. Comput. Phys. 348, 271–297.
Debenedetti, P.G., 2020. Metastable Liquids: Concepts and Principles. Princeton University Press.
Deike, L., 2022. Mass transfer at the ocean–atmosphere interface: The role of wave breaking, droplets, and bubbles. Ann. Rev. Fluid Mech. 54, 191–224.
Dieter-Kissling, K., Marschall, H., Bothe, D., 2015. Numerical method for coupled interfacial surfactant transport on dynamic surface meshes of general topology. Comput. & Fluids 109, 168–184.
Dollet, B., Marmottant, P., Garbin, V., 2019. Bubble dynamics in soft and biological matter. Annu. Rev. Fluid. Mech. 51, 331–355.
Duhar, G., Colin, C., 2006. Dynamics of bubble growth and detachment in a viscous shear flow. Phys. Fluids 18 (7), 077101.
Ellingsen, K., Risso, F., 2001. On the rise of an ellipsoidal bubble in water: oscillatory paths and liquid-induced velocity. J. Fluid Mech. 440, 235–268.
Ern, P., Risso, F., Fabre, D., Magnaudet, J., 2012. Wake-induced oscillatory paths of bodies freely rising or falling in fluids. Annu. Rev. Fluid Mech. 44, 97–121.
Errico, C., Pierre, J., Pezet, S., Desailly, Y., Lenkei, Z., Couture, O., Tanter, M., 2015. Ultrafast ultrasound localization microscopy for deep super-resolution vascular imaging. Nature 527, 499–502.
Ervin, E., Tryggvason, G., 1997. The rise of bubbles in a vertical shear flow. ASME J. Fluid Eng. 119, 443–449.
Esmaeeli, A., Tryggvason, G., 2005. A DNS study of the buoyant rise of bubbles at o(100) Reynolds numbers. Phys. Fluids 17, 093303.
Estrada, J.B., Barajas, C., Henann, D.L., Johnsen, E., Franck, C., 2018. High strain-rate soft material characterization via inertial cavitation. J. Mech. Phys. Solids 112, 291–317.
Falcone, M., Bothe, D., Marschall, H., 2018. 3D direct numerical simulations of reactive mass transfer from deformable single bubbles: An analysis of mass transfer coefficients and reaction selectivities. Chem. Eng. Sci. 177, 523–536.
Faraday, M., 2005. The Chemical History of a Candle. Barnes & Noble Publishing.
Favre, L., Colin, C., Pujet, S., Mimouni, S., 2023. An updated force balance approach to investigate bubble sliding in vertical flow boiling at low and high pressures. Int. J. Heat Mass Transfer 211, 124227.
Figueroa-Espinoza, B., Mena, B., Aguilar-Corona, A., Zenit, R., 2018. The lifespan of clusters in confined bubbly liquids. Int. J. Multiph. Flow 106, 138–146.
Fischer, S., Gambaryan-Roisman, T., Stephan, P., 2015. On the development of a thin evaporating liquid film at a receding liquid/vapour-interface. Int. J. Heat Mass Transfer 88, 346–356.
Fleckenstein, S., Bothe, D., 2015. A volume-of-fluid-based numerical method for multi-component mass transfer with local volume changes. J. Comput. Phys. 301, 35–58.
Fogler, H.S., Goddard, J.D., 1970. Collapse of spherical cavities in viscoelastic fluids. Phys. Fluids 13 (5), 1135–1141.
Fraggedakis, D., Pavlidis, M., Dimakopoulos, Y., Tsamopoulos, J., 2016. On the velocity discontinuity at a critical volume of a bubble rising in a viscoelastic fluid. J. Fluid Mech. 789, 310–346.
Fritz, W., 1935. Berechnung des Maximalvolumens von Dampfblasen. Phys. Z. 11, 379–384.
Funfschilling, D., Li, H., 2001. Flow of non-Newtonian fluids around bubbles: PIV measurements and birefringence visualisation. Chem. Eng. Sci. 56 (3), 1137–1141.
Gaitan, D.F., 1990. An Experimental Investigation of Acoustic Cavitation in Gaseous Liquids (Ph.D. thesis). The University of Mississippi.
Gaitan, D.F., Crum, L.A., Church, C.C., Roy, R.A., 1992. Sonoluminescence and bubble dynamics for a single, stable, cavitation bubble. J. Acoust. Soc. Am. 91 (6), 3166–3183.
Gallo, M., Magaletti, F., Casciola, C.M., 2018. Thermally activated vapor bubble nucleation: The Landau-Lifshitz–Van der Waals approach. Phys. Rev. Fluids 3 (5), 053604.
Gallo, M., Magaletti, F., Casciola, C.M., 2021. Heterogeneous bubble nucleation dynamics. J. Fluid Mech. 906, A20.
Gallo, M., Magaletti, F., Georgoulas, A., Marengo, M., De Coninck, J., Casciola, C.M., 2023. A nanoscale view of the origin of boiling and its dynamics. Nat. Commun. 14 (1), 6428.
Ganesan, S., Tobiska, L., 2012. Arbitrary Lagrangian–Eulerian finite-element method for computation of two-phase flows with soluble surfactants. J. Comput. Phys. 231 (9), 3685–3702.
Gaudron, R., Warnez, M., Johnsen, E., 2015. Bubble dynamics in a viscoelastic medium with nonlinear elasticity. J. Fluid Mech. 766 (1), 54–75.
Gennari, G., Smith, E.R., Pringle, G.J., Magnini, M., 2024. Coupled atomistic–continuum simulations of nucleate boiling. Int. J. Therm. Sci. 200.
Giacomello, A., Chinappi, M., Meloni, S., Casciola, C.M., 2013. Geometry as a catalyst: How vapor cavities nucleate from defects. Langmuir 29 (48), 14873–14884.
Giles, B.F., 1968. Pneumatic acoustic energy source. Geophys. Prospect. 16 (1), 21–53.
Gilman, L., Baglietto, E., 2017. A self-consistent, physics-based boiling heat transfer modeling framework for use in computational fluid dynamics. Int. J. Multiph. Flow 95, 35–53.
van Gils, D.P.M., Narezo Guzman, D., Sun, C., Lohse, D., 2013. The importance of bubble deformability for strong drag reduction in bubbly turbulent Taylor-Couette flow. J. Fluid Mech. 722, 317–347.
Grossmann, S., Lohse, D., Sun, C., 2016. High–Reynolds number Taylor–Couette turbulence. Annu. Rev. Fluid Mech. 48, 53–80.
Gründing, D., Fleckenstein, S., Bothe, D., 2016. A subgrid-scale model for reactive concentration boundary layers for 3D mass transfer simulations with deformable fluid interfaces. Int. J. Heat Mass Transfer 101, 476–487.
Guelfi, A., Bestion, D., Boucker, M., Boudier, P., Fillion, P., Grandotto, M., Hérard, J.-M., Hervieu, E., Péturaud, P., 2007. NEPTUNE: A new software platform for advanced nuclear thermal hydraulics. Nucl. Sci. Eng. 156 (3), 281–324.
Guido, B., Yuki, S., Arwen II, T., Oscar, C., et al., 2016. Mechanical characterization of ultralow interfacial tension oil-in-water droplets by thermal capillary wave analysis in a microfluidic device.
Haghani-Hassan-Abadi, R., Fakhari, A., Rahimian, M.H., 2021. Phase-change modeling based on a novel conservative phase-field method. J. Comput. Phys. 432.
Haghnegahdar, M., Boden, S., Hampel, U., 2016. Investigation of surfactant effect on the bubble shape and mass transfer in a milli-channel using high-resolution microfocus X-ray imaging. Int. J. Multiph. Flow 87, 184–196.
Harlen, O., 2002. The negative wake behind a sphere sedimenting through a viscoelastic fluid. J. Non-Newton. Fluid Mech. 108 (1–3), 411–430.
Haroun, Y., Legendre, D., Raynal, L., 2010. Volume of fluid method for interfacial reactive mass transfer: Application to stable liquid film. Chem. Eng. Sci. 65 (10), 2896–2909.
Hassager, O., 1979. Negative wake behind bubbles in non-newtonian liquids. Nature 279 (5712), 402–403.
Hayashi, K., Tomiyama, A., 2011. Interface tracking simulation of mass transfer from a dissolving bubble. J. Comput. Multiph. Flows 3 (4), 247–261.
Hebrard, G., Zeng, J., Loubiere, K., 2009. Effect of surfactants on liquid side mass transfer coefficients: a new insight. Chem. Eng. J. 148 (1), 132–138.
Helfield, B., Chen, X., Watkins, S.C., Villanueva, F.S., 2016. Biophysical insight into mechanisms of sonoporation. Proc. Natl. Acad. Sci. 113 (36), 9983–9988.
Hibiki, T., Ishii, M., 2003. Active nucleation site density in boiling systems. Int. J. Heat Mass Transfer 46, 2587–2601.
Hidman, N., Ström, H., Sasic, S., Sardina, G., 2022. The lift force on deformable and freely moving bubbles in linear shear flows. J. Fluid Mech. 952, A34.
Hilgenfeldt, S., Grossmann, S., Lohse, D., 1999. A simple explanation of light emission in sonoluminescence. Nature 398 (6726), 402–405.
Hilgenfeldt, S., Lohse, D., Brenner, M.P., 1996. Phase diagrams for sonoluminescing bubbles. Phys. Fluids 8 (11), 2808–2826.
Hori, Y., Bothe, D., Hayashi, K., Hosokawa, S., Tomiyama, A., 2020. Mass transfer from single carbon-dioxide bubbles in surfactant-electrolyte mixed aqueous solutions in vertical pipes. Int. J. Multiph. Flow 124, 103207.
Hori, Y., Hirota, Y., Hayashi, K., Hosokawa, S., Tomiyama, A., 2019. Combined effects of alcohol and electrolyte on mass transfer from single carbon-dioxide bubbles in vertical pipes. Int. J. Heat Mass Transfer 136, 521–530.
Horowitz, M., Williamson, C., 2010. The effect of Reynolds number on the dynamics and wakes of freely rising and falling spheres. J. Fluid Mech. 651, 251–294.
Hsu, Y.Y., 1962. On the size range of active nucleation cavities on a heating surface. J. Heat Transf. 84, 207–213.
Hua, C., Johnsen, E., 2013. Nonlinear oscillations following the Rayleigh collapse of a gas bubble in a linear viscoelastic (tissue-like) medium. Phys. Fluids 25 (8), 083101.
Huber, G., Tanguy, S., Sagan, M., Colin, C., 2017. Direct numerical simulation of nucleate pool boiling at large microscopic contact angle and moderate Jakob number. Int. J. Heat Mass Transfer 113, 662–682.
Jamburidze, A., De Corato, M., Huerre, A., Pommella, A., Garbin, V., 2017. High-frequency linear rheology of hydrogels probed by ultrasound-driven microbubble dynamics. Soft Matter 13, 3946–3953.
James, A., Lowengrub, J., 2004. A surfactant-conserving volume-of-fluid method for interfacial flows with insoluble surfactant. J. Comput. Phys. 201 (2), 685–722.
Janecek, V., Nikolayev, V.S., 2012. Contact line singularity at partial wetting during evaporation driven by substrate heating. EPL 100 (1), 14003.

Jensen, K.H., Berg-Sørensen, K., Bruus, H., Holbrook, N.M., Liesche, J., Schulz, A., Zwieniecki, M.A., Bohr, T., 2016. Sap flow and sugar transport in plants. Rev. Modern Phys. 88 (3), 035007.
Jiang, H., Liu, Y., Chu, H., 2023. A review of numerical investigation on pool boiling. J. Therm. Anal. Calorim. 148, 8697–8745.
Jiang, X., Rotily, L., Villermaux, E., Wang, X., 2024. Abyss aerosols: Drop production from underwater bubble collisions. Phys. Rev. Lett. 133 (2), 024001.
Jiang, N., Xie, B., Zhang, X., He, M., Li, K., Bai, J., Wang, Z., He, J., Zhang, L., 2014. Enhancing ablation effects of a microbubble-enhancing contrast agent ("SonoVue") in the treatment of uterine fibroids with high-intensity focused ultrasound: A randomized controlled trial. Cardiovasc. Intervent. Radiol. 37 (5), 1321–1328.
Jiménez-Fernández, J., Crespo, A., 2005. Bubble oscillation and inertial cavitation in viscoelastic fluids. Ultrasonics 43 (8), 643–651.
Jin, Y., Schlüter, M., 2019. Direct numerical simulation of the interfacial mass transfer of a bubble in self-induced turbulent flows. Int. J. Heat Mass Transfer 135, 1248–1259.
Jung, S., Kim, H., 2018. Hydrodynamic formation of a microlayer underneath a boiling bubble. Int. J. Heat Mass Transfer 120, 1229–1240.
Juniper, M., Noakes, C., Tobias, S., Savy, C., Lincoln, J., 2021. Our fluid nation: the impact of fluid dynamics on the UK. Tech. Rep., UK Fluids Network.
Karapetsas, G., Photeinos, D., Dimakopoulos, Y., Tsamopoulos, J., 2019. Dynamics and motion of a gas bubble in a viscoplastic medium under acoustic excitation. J. Fluid Mech. 865, 381–413.
Kashchiev, D., 2000. Nucleation. Elsevier.
Kentheswaran, K., Antier, W., Dietrich, N., Lalanne, B., 2023. Impact of surfactants on the rise of deformable bubbles and interfacial gas–liquid mass transfer. J. Fluid Mech. 970, A5.
Kentheswaran, K., Dietrich, N., Tanguy, S., Lalanne, B., 2022. Direct numerical simulation of gas-liquid mass transfer around a spherical contaminated bubble in the stagnant-cap regime. Int. J. Heat Mass Transfer 198, 123325.
Ketterling, J.A., Apfel, R.E., 1998. Experimental validation of the dissociation hypothesis for single bubble sonoluminescence. Phys. Rev. Lett. 81 (22), 4991–4994.
Kharangate, C.R., Mudawar, I., 2017. Review of computational studies on boiling and condensation. Int. J. Heat Mass Transfer 108, 1164–1196.
Kochkov, D., Smith, J.A., Alieva, A., Wang, Q., Brenner, M.P., Hoyer, S., 2021. Machine learning–accelerated computational fluid dynamics. Proc. Nat. Acad. Sci. 118 (21), e2101784118.
Koynov, A., Khinast, J., Tryggvason, G., 2005a. Mass transfer and chemical reactions in bubble swarms with dynamic interfaces. AIChE J. 51 (10), 2786–2800.
Koynov, A., Tryggvason, G., Khinast, J.G., 2005b. Mass transfer and chemical reactions in bubble swarms with dynamic interfaces. AIChE J. 10, 2786–2800.
Kramers, H.A., 1940. Brownian motion in a field of force and the diffusion model of chemical reactions. Physica 7 (4), 284–304.
Krasovitski, B., Frenkel, V., Shoham, S., Kimmel, E., 2011. Intramembrane cavitation as a unifying mechanism for ultrasound-induced bioeffects. Proc. Natl. Acad. Sci. 108 (8), 3258–3263.
Kunkelmann, C., Stephan, P., 2010. Numerical simulation of the transient heat transfer during nucleate boiling of refrigerant HFE-7100. Int. J. Refrig. 33 (7), 1221–1228.
Kurul, N., Podowski, M.Z., 1991. On the modeling of multi-dimensional effects in boiling channels. 27th Natl. Heat Transf. Conf..
Laaksonen, A., Talanquer, V., Oxtoby, D.W., 1995. Nucleation: measurements, theory, and atmospheric applications.. Annu. Rev. Phys. Chem. 46, 489–524.
Landau, L., Lifshitz, E., 1980. Statistical physics, vol. 5. Course Theor. Phys. 30.
Lee, J., Pozrikidis, C., 2006. Effect of surfactants on the deformation of drops and bubbles in Navier–Stokes flow. Comput. & Fluids 35 (1), 43–60.
Lefèvre, F., Masri, M.A., Ibrahim, J., Veillas, C., Verrier, I., Celle, F., Parriaux, O., Jourlin, Y., Cioulachtjian, S., 2022. Plasmon resonance measurements in pool boiling, condensation and evaporation experiments on a nanostructured surface. Int. J. Heat Mass Transfer 184.
Legendre, D., Boree, J., Magnaudet, J., 1998. Thermal and dynamic evolution of a spherical bubble moving steadily in a superheated or subcooled liquid. Phys. Fluids 10 (6), 1256–1272.
Lehrenfeld, C., Reusken, A., 2012. Nitsche-XFEM with streamline diffusion stabilization for a two-phase mass transport problem. SIAM J. Sci. Comput. 34 (5), A2740–A2759.
Lentacker, I., De Cock, I., Deckers, R., De Smedt, S.C., Moonen, C.T.W., 2014. Understanding ultrasound induced sonoporation: Definitions and underlying mechanisms. Adv. Drug Deliv. Rev. 72, 49–64.
Lhuissier, H., Villermaux, E., 2012. Bursting bubble aerosols. J. Fluid Mech. 696, 5–44.
Li, Q., Jiao, Y., Avramova, M., Chen, P., Yu, J., Chen, J., Hou, J., 2018. Development, verification and application of a new model for active nucleation site density in boiling systems. Nucl. Eng. Des. 328, 1–9.
Li, S., van der Meer, D., Zhang, A.-M., Prosperetti, A., Lohse, D., 2020. Modelling large scale airgun-bubble dynamics with highly non-spherical features. Int. J. Multiph. Flow 122, 103143.
Liger-Belair, G., 2005. The physics and chemistry behind the bubbling properties of champagne and sparkling wines: a state-of-the-art review. J. Agricult. Food Chem. 53 (8), 2788–2802.
Liu, H., Ahmad, S., Chen, J., Zhao, J., 2020. Molecular dynamics study of the nanoscale boiling heat transfer process on nanostructured surfaces. Int. Commun. Heat Mass Transfer 119.
Liu, T.J., Bankoff, S.G., 1993. Structure of air-water bubbly flow in a vertical pipe–I. Liquid mean velocity and turbulence measurements. Int. Commun. Heat Mass Transfer 36, 1049–1060.
Lohse, D., 2018. Bubble puzzles: From fundamentals to applications. Phys. Rev. Fluids 3 (10), 110504.
Lohse, D., 2022. Fundamental fluid dynamics challenges in inkjet printing. Annu. Rev. Fluid Mech. 54, 349–382.
Lohse, D., Brenner, M.P., Dupont, T.F., Hilgenfeldt, S., Johnston, B., 1997. Sonoluminescing air bubbles rectify argon. Phys. Rev. Lett. 78 (7), 1359–1362.
Lohse, D., Henkes, R., Lincoln, J., Wullems, R., 2023. Flow to the Future – Fluid Dynamics in the Netherlands. Tech. Rep., J.M. Burgerscentrum.
Lohse, D., Villermaux, E., 2020. Double threshold behavior for breakup of liquid sheets. Proc. Nat. Acad. Sci. 117 (32), 18912–18914.
Lohse, D., Zhang, X., 2015. Surface nanobubbles and nanodroplets. Rev. Modern Phys. 87, 981–1035.
Lu, J., Biswas, S., Tryggvason, G., 2006. A DNS study of laminar bubbly flows in a vertical channel. Int. J. Multiph. Flow 32, 643–660.
Lu, J., Fernandez, A., Tryggvason, G., 2005. The effect of bubbles on the wall shear in a turbulent channel flow. Phys. Fluids 17, 095102.
Lu, J., Muradoglu, M., Tryggvason, G., 2017. Effect of insoluble surfactant on turbulent bubbly flows in vertical channels. Int. J. Multiph. Flow 95, 135–143.
Lu, J., Tryggvason, G., 2006. Numerical study of turbulent bubbly downflows in a vertical channel. Phys. Fluids 18, 10, 103302.
Lu, J., Tryggvason, G., 2007. Effect of bubble size in turbulent bubbly downflow in a vertical channel. Chem. Eng. Sci. 62, 3008–3018.
Lu, J., Tryggvason, G., 2008. Effect of bubble deformability in turbulent bubbly upflow in a vertical channel. Phys. Fluids 20, 040701.
Lu, J., Tryggvason, G., 2013. Dynamics of nearly spherical bubbles in a turbulent channel upflow. J. Fluid Mech. 732, 166–189.
Lu, J., Tryggvason, G., 2018. Direct numerical simulations of multifluid flows in a vertical channel undergoing topology changes. Phys. Rev. Fluids 3, 20, 084401.
Lu, J., Tryggvason, G., 2019. Multifluid flows in a vertical channel undergoing topology changes–effect of void fraction. Phys. Rev. Fluids 4, 084301.
Lutsko, J.F., 2008. Density functional theory of inhomogeneous liquids. III. Liquid-vapor nucleation. J. Chem. Phys. 129.
Maarek, J., 2024. Mass Transfer at Fluid Interfaces at Large Péclet Numbers (Ph.D. thesis). Sarbonne Université, Institut Jean le Rond d'Alembert Modeling and Analysis.
Maes, J., Soulaine, C., 2018. A new compressive scheme to simulate species transfer across fluid interfaces using the Volume-Of-Fluid method. Chem. Eng. Sci. 190, 405–418.
Maes, J., Soulaine, C., 2020. A unified single-field Volume-of-Fluid-based formulation for multi-component interfacial transfer with local volume changes. J. Comput. Phys. 402, 109024.
Magaletti, F., Gallo, M., Casciola, C.M., 2021. Water cavitation from ambient to high temperatures. Sci. Rep. 11 (1), 20801.
Magaletti, F., Georgoulas, A., Marengo, M., 2020. Unraveling low nucleation temperatures in pool boiling through fluctuating hydrodynamics simulations. Int. J. Multiph. Flow 130.
Magnaudet, J., Eames, I., 2000. The motion of high-Reynolds number bubbles in inhomogeneous flows. Annu. Rev. Fluid Mech. 32, 659–708.
Marengo, M., Coninck, J.D., 2022. The Surface Wettability Effect on Phase Change. Springer International Publishing, Cham,
Marie, A., Cioulachtjian, S., Lips, S., Sartre, V., 2022. Thermal interactions between nucleation sites and the solid wall during pool boiling of a pure fluid: A review. Int. J. Therm. Sci. 174, 107388.
Marmottant, P., van der Meer, S., Emmer, M., Versluis, M., de Jong, N., Hilgenfeldt, S., Lohse, D., 2005. A model for large amplitude oscillations of coated bubbles accounting for buckling and rupture. J. Acoust. Soc. Am. 118 (6), 3499–3505.
Marschall, H., Hinterberger, K., Schüler, C., Habla, F., Hinrichsen, O., 2012. Numerical simulation of species transfer across fluid interfaces in free-surface flows using OpenFOAM. Chem. Eng. Sci. 78, 111–127.
Martínez Mercado, J., Chehata Gomez, D., Van Gils, D., Toschi, F., Lohse, D., 2010. On bubble clustering and energy spectra in pseudo-turbulence. J. Fluid Mech. 650, 287.
Mathijssen, A.J., Lisicki, M., Prakash, V.N., Mossige, E.J., 2023. Culinary fluid mechanics and other currents in food science. Rev. Modern Phys. 95 (2), 025004.
Matsumoto, M., Tanaka, K., 2008. Nano bubble—Size dependence of surface tension and inside pressure. Fluid Dyn. Res. 40, 546.
Maxey, M.R., Riley, J.J., 1983. Equation of motion for a small rigid sphere in a nonuniform flow. Phys. Fluids 26, 883–889.
Mazzocco, T., Ambrosini, W., Kommajosyula, R., Baglietto, E., 2018. A reassessed model for mechanistic prediction of bubble departure and lift off diameters. Int. J. Heat Mass Transfer 117, 119–124.
Meijer, J.G., Rocha, D., Linnenbank, A.M., Diddens, C., Lohse, D., 2024. Enhanced bubble growth near an advancing solidification front. J. Fluid Mech. 996, A22.

Menzl, G., Gonzalez, M.A., Geiger, P., Caupin, F., Abascal, J.L., Valeriani, C., Dellago, C., 2016. Molecular mechanism for cavitation in water under tension. Proc. Natl. Acad. Sci. 113 (48), 13582–13587.
Mezui, Y., Cartellier, A., Obligado, M., 2023. An experimental study on the liquid phase properties of a bubble column operated in the homogeneous and in the heterogeneous regimes. Chem. Eng. Sci. 268, 118381.
Mezui, Y., Obligado, M., Cartellier, A., 2022. Buoyancy-driven bubbly flows: scaling of velocities in bubble columns operated in the heterogeneous regime. J. Fluid Mech. 952, A10.
Mikic, B., Rohsenow, W.M., Griffith, P., 1970. On bubble growth rates. Int. J. Heat Mass Transfer 13, 657–666.
Mougin, G., Magnaudet, J., 2002. Path instability of a rising bubble. Phys. Rev. Lett. 88, 014502.
Mudde, R.F., 2005. Gravity-driven bubbly flows. Annu. Rev. Fluid Mech. 37 (1), 393.
Muradoglu, M., Tryggvason, G., 2008. A front-tracking method for computation of interfacial flows with soluble surfactants. J. Comput. Phys. 227 (4), 2238–2262.
Muradoglu, M., Tryggvason, G., 2014. Simulations of soluble surfactants in 3D multiphase flow. J. Comput. Phys. 274, 737–757.
Nam, Y., Ju, Y.S., 2008. Bubble nucleation on hydrophobic islands provides evidence to anomalously high contact angles of nanobubbles. Appl. Phys. Lett. 93, 103115.
Naude, J., Méndez, F., 2008. Periodic and chaotic acoustic oscillations of a bubble gas immersed in an upper convective Maxwell fluid. J. Non-Newton. Fluid Mech. 155 (1), 30–38.
Nekoeian, S., Aghajani, M., Alavi, S., Sotoudeh, F., 2019. Effect of surfactants on mass transfer coefficients in bubble column contactors: an interpretative critical review study. Rev. Chem. Eng. 20180089.
Niethammer, M., Brenn, G., Marschall, H., D., B., 2019. An extended volume of fluid method and its application to single bubbles rising in a viscoelastic liquid. J. Comput. Phys 387, 326–355.
Nikolayev, V.S., 2021. Physical principles and state-of-the-art of modeling of the pulsating heat pipe: A review. Appl. Therm. Eng. 195, 117111.
Noé, F., Tkatchenko, A., Müller, K.-R., Clementi, C., 2020. Machine learning for molecular simulation. Annu. Rev. Phys. Chem..
Ohl, C.-D., Arora, M., Ikink, R., de Jong, N., Versluis, M., Delius, M., Lohse, D., 2006. Sonoporation from jetting cavitation bubbles. Biophys. J. 91 (11), 4285–4295.
Onea, A., Wörner, M., Cacuci, D., 2009. A qualitative computational study of mass transfer in upward bubble train flow through square and rectangular mini-channels. Chem. Eng. Sci. 64 (7), 1416–1435.
Oratis, A.T., Dijs, K., Lajoinie, G., Versluis, M., Snoeijer, J.H., 2024. A unifying Rayleigh-Plesset-type equation for bubbles in viscoelastic media. J. Acoust. Soc. Am. 155, 1593–1605.
Panda, A., Peters, E., Baltussen, M., Kuipers, J., 2019. Fully resolved scalar transport for high Prandtl number flows using adaptive mesh refinement. Chem. Eng. Sci.: X 4, 100047.
Pandey, V., Mitra, D., Perlekar, P., 2022. Turbulence modulation in buoyancy-driven bubbly flows. J. Fluid Mech. 932, A19.
Pandey, V., Ramadugu, R., Perlekar, P., 2020. Liquid velocity fluctuations and energy spectra in three-dimensional buoyancy-driven bubbly flows. J. Fluid Mech. 884, R6.
Park, S., Liu, L., Demirkır, c., van der Heijden, O., Lohse, D., Krug, D., Koper, M.T., 2023. Solutal Marangoni effect determines bubble dynamics during electrocatalytic hydrogen evolution. Nat. Chem. 15 (11), 1532–1540.
Paul, S., Hsu, W.-L., Magnini, M., Mason, L.R., Ho, Y.-L., Matar, O.K., Daiguji, H., 2020. Single-bubble dynamics in nanopores: Transition between homogeneous and heterogeneous nucleation. Phys. Rev. Res. 2, 43400.
Peleka, E.N., Gallios, G.P., Matis, K.A., 2018. A perspective on flotation: A review. J. Chem. Technol. Biotechnol. 93 (3), 615–623.
Pereno, V., Aron, M., Vince, O., Mannaris, C., Seth, A., De Saint Victor, M., Lajoinie, G., Versluis, M., Coussios, C., Carugo, D., Stride, E., 2018. Layered acoustofluidic resonators for the simultaneous optical and acoustic characterisation of cavitation dynamics, microstreaming, and biological effects. Biomicrofluidics 12 (3).
Pesci, C., Weiner, A., Marschall, H., Bothe, D., 2018. Computational analysis of single rising bubbles influenced by soluble surfactant. J. Fluid Mech. 856, 709–763.
Pilz, C., Brenn, G., 2007. On the critical bubble volume at the rise velocity jump discontinuity in viscoelastic liquids. J. Non-Newton. Fluid Mech. 145 (2–3), 124–138.
Plesset, M.S., Prosperetti, A., 1977. Bubble dynamics and cavitation. Annu. Rev. Fluid Mech. 9, 145–185.
Plesset, S.A., 1953. The growth of vapor bubbles in superheated liquids. J. Appl. Phys. 25 (4).
Popinet, S., 2014. Basilisk. URL: http://basilisk.fr.
Popinet, S., 2018. Numerical models of surface tension. Annu. Rev. Fluid Mech. 50, 49–75.
Prosperetti, A., 1977a. Thermal effects and damping mechanisms in the forced radial oscillations of gas bubbles in liquid. J. Acoust. Soc. Am. 61, 17–27.
Prosperetti, A., 1977b. Viscous effects on perturbed spherical flows. Quart. Appl. Math. 34, 339–350.
Prosperetti, A., 2004. Bubbles. Phys. Fluids 16, 1852–1865.
Prosperetti, A., 2017. Vapor bubbles. Ann. Rev. Fluid Mech. 49 (1), 221–248.
Prosperetti, A., Crum, L.A., Commander, K.W., 1988. Nonlinear bubble dynamics. J. Acoust. Soc. Am. 83 (2), 502–514.
Qi, Y., Klausner, J.F., 2005. Comparison of nucleation site density for pool boiling and gas nucleation. J. Heat Transf. 128, 13–20.
Radl, S., Koynov, A., Tryggvason, G., Khinast, J.G., 2008. DNS-based prediction of the selectivity of fast multiphase reactions: Hydrogenation of nitroarenes. Chem. Eng. Sci. 63, 3279–3291.
Ramirez, G., Burlot, A., Zamansky, R., Bois, G., Risso, F., 2024. Spectral analysis of dispersed multiphase flows in the presence of fluid interfaces. Int. J. Multiph. Flow 104860.
Ran, Y., Bertola, V., 2024. Achievements and prospects of molecular dynamics simulations in thermofluid sciences. Energies 17.
Rednikov, A., Colinet, P., 2013. Singularity-free description of moving contact lines for volatile liquids. Phys. Rev. E 87 (1), 010401.
Ren, W., Vanden-Eijnden, E., et al., 2007. Simplified and improved string method for computing the minimum energy paths in barrier-crossing events. J. Chem. Phys. 126 (16).
Riboux, G., Legendre, D., Risso, F., 2013. A model of bubble-induced turbulence based on large-scale wake interactions. J. Fluid Mech. 719, 362–387.
Riboux, G., Risso, F., Legendre, D., 2010. Experimental characterization of the agitation generated by bubbles rising at high Reynolds number. J. Fluid Mech. 643, 509–539.
Richenderfer, A., Kossolapov, A., Seong, J.H., Saccone, G., Demarly, E., Kommajosyula, R., Baglietto, E., Buongiorno, J., Bucci, M., 2018. Investigation of subcooled flow boiling and CHF using high-resolution diagnostics. Exp. Therm. Fluid Sci. 99, 35–58.
Risso, F., 2018. Agitation, mixing, and transfers induced by bubbles. Annu. Rev. Fluid Vol. 43 50 (1), 25–48.
Risso, F., Roig, V., Amoura, Z., Riboux, G., Billet, A.-M., 2008. Wake attenuation in large Reynolds number dispersed two-phase flows.. Philos. Trans. Ser. A, Math. Phys. Eng. Sci. 366 (1873), 2177–2190.
Roghair, I., Annaland, M.V.S., Kuipers, J., 2016. An improved front-tracking technique for the simulation of mass transfer in dense bubbly flows. Chem. Eng. Sci. 152, 351–369.
Rosen, M.J., Wang, H., Shen, P., Zhu, Y., 2005. Ultralow interfacial tension for enhanced oil recovery at very low surfactant concentrations. Langmuir 21 (9), 3749–3756.
Ruckenstein, E., Davis, J.E., 1971. The effects of bubble translation on vapor on vapor bubble growth in a superheated liquid. Int. J. Heat Mass Transfer 14, 939–952.
Saint-Michel, B., Garbin, V., 2020a. Acoustic bubble dynamics in a yield-stress fluid. Soft Matter 16, 10405–10418.
Saint-Michel, B., Garbin, V., 2020b. Bubble dynamics for broadband microrheology of complex fluids. Curr. Opin. Colloid & Interface Sci. 50, 101392.
Salvalaglio, M., Tiwary, P., Maggioni, G.M., Mazzotti, M., Parrinello, M., 2016. Overcoming time scale and finite size limitations to compute nucleation rates from small scale well tempered metadynamics simulations. J. Chem. Phys. 145, 211925.
Sardeing, R., Painmanakul, P., Hébrard, G., 2006. Effect of surfactants on liquid-side mass transfer coefficients in gas–liquid systems: a first step to modeling. Chem. Eng. Sci. 61 (19), 6249–6260.
Sato, Y., Niceno, B., 2018. Pool boiling simulation using an interface tracking method: From nucleate boiling to film boiling regime through critical heat flux. Int. J. Heat Mass Transfer 125, 876–890.
Schlüter, M., Herres-Pawlis, S., Nieken, U., Tuttlies, U., Bothe, D., 2021. Small-scale phenomena in reactive bubbly flows: Experiments, numerical modeling, and applications. Annu. Rev. Chem. Biomol. Eng. 12, 625–643.
Schmelzer, J.W., 2001. Comments on the nucleation theorem. J. Colloid Interface Sci. 242, 354–372.
Schweikert, K., Sielaff, A., Stephan, P., 2019. On the transition between contact line evaporation and microlayer evaporation during the dewetting of a superheated wall. Int. J. Therm. Sci. 145, 106025.
Scriven, L.E., 1959. On the dynamics of phase growth. Chem. Eng. Sci. 1–13.
Serizawa, A., Kataoka, I., Michiyoshi, I., 1975. Turbulence structure of air-water bubbly flow–II. Local properties. Int. J. Multiph. Flow 2, 235–246.
Shahmardi, A., Tammisola, O., Chinappi, M., Brandt, L., 2021. Effects of surface nanostructure and wettability on pool boiling: A molecular dynamics study. Int. J. Therm. Sci. 167.
Shi, P., Rzehak, R., Lucas, D., Magnaudet, J., 2020. Hydrodynamic forces on a clean spherical bubble translating in a wall-bounded linear shear flow. Phys. Rev. Fluids 5 (7), 073601.
Shin, S., Chergui, J., Juric, D., Kahouadji, L., Matar, O., Craster, R., 2018. A hybrid interface tracking–level set technique for multiphase flow with soluble surfactant. J. Comput. Phys. 359, 409–435.
Sielaff, A., Mangini, D., Kabov, O., Raza, M., Garivalis, A., Zupanã, M., Dehaeck, S., Evgenidis, S., Jacobs, C., Van Hoof, D., Oikonomidou, O., Zabulis, X., Karamaounas, P., Bender, A., Ronshin, F., Schinnerl, M., Sebilleau, J., Colin, C., Di Marco, P., Karapantsios, T., Golobiã, I., Rednikov, A., Colinet, P., Stephan, P., Tadrist, L., 2022. The multiscale boiling investigation on-board the international space station: An overview. Appl. Therm. Eng. 205, 117932.
Situ, R., Hibiki, T., Ishii, M., Mori, M., 2005. Bubble lift-off size in forced convective subcooled boiling flow. Int. J. Heat Mass Transfer 48 (25–26), 5536–5548.

Sodtke, C., Kern, J., Schweizer, N., Stephan, P., 2006. High resolution measurements of wall temperature distribution underneath a single vapour bubble under low gravity conditions. Int. J. Heat Mass Transfer 49 (5–6), 1100–1106.
Son, G., Dhir, V.K., Ramanujapu, N., 1999. Dynamics and heat transfer associated with a single bubble during nucleate boiling on a horizontal surface. J. Heat Transf. 121, 631.
Spandan, V., Lohse, D., de Tullio, M.D., Verzicco, R., 2018a. A fast moving least squares approximation with adaptive Lagrangian mesh refinement for large scale immersed boundary simulations. J. Comput. Phys. 375, 228–239.
Spandan, V., Verzicco, R., Lohse, D., 2018b. Physical mechanisms governing drag reduction in turbulent Taylor–Couette flow with finite-size deformable bubbles. J. Fluid Mech. 849, R3.
Stephan, P., Busse, C., 1992. Analysis of the heat transfer coefficient of grooved heat pipe evaporator walls. Int. J. Heat Mass Transfer 35 (2), 383–391.
Stojanović, A.D., Belosević, S.V., Crnomarković, N.D., Tomanović, I.D., Milićević, A.R., 2022. Nucleate pool boiling heat transfer review of models and bubble dynamics parameters. Therm. Sci. 26, 157–174.
Tachibana, K., Tachibana, S., 1995. Albumin microbubble echo-contrast material as an enhancer for ultrasound accelerated thrombolysis. Circulation 92 (5), 1148–1150.
Takagi, S., Matsumoto, Y., 2011. Surfactant effects on bubble motion and bubbly flows. Annu. Rev. Fluid Mech. 43, 615–636.
Takagi, S., Ogasawara, T., Matsumoto, Y., 2008. The effects of surfactant on the multiscale structure of bubbly flows. Philos. Trans. R. Soc. A: 366, 2117–2129.
Tchoufag, J., Fabre, D., Magnaudet, J., 2014a. Global linear stability analysis of the wake and path of buoyancy-driven disks and thin cylinders. J. Fluid Mech. 740, 278–311.
Tchoufag, J., Magnaudet, J., Fabre, D., 2014b. Linear instability of the path of a freely rising spheroidal bubble. J. Fluid Mech. 751, R4.
Tecchio, C., Zhang, X., Cariteau, B., Zalczer, G., Roca I Cabarrocas, P., Bulkin, P., Charliac, J., Vassant, S., Nikolayev, V.S., 2024. Microlayer in nucleate boiling seen as Landau–Levich film with dewetting and evaporation. J. Fluid Mech. 989, A4.
Thorncroft, G., Klausner, F., Mei, R., 2001. Bubble forces and detachment models. Multiph. Sci. Technol. 13 (3 & 4), 35–76.
Toegel, R., Lohse, D., 2003. Phase diagrams for sonoluminescing bubbles: A comparison between experiment and theory. J. Chem. Phys. 118, 1863.
Tolman, R.C., 1949. The effect of droplet size on surface tension. J. Chem. Phys. 17 (3), 333–337.
Tomiyama, A., Tamai, H., Zun, I., Hosokawa, S., 2002. Transverse migration of single bubbles in simple shear flows. Chem. Eng. Sci. 57, 1849–1858.
Torres, L., Urbano, A., Colin, C., Tanguy, S., 2024. On the coupling between direct numerical simulation of nucleate boiling and a micro-region model at the contact line. J. Comput. Phys. 497, 112602.
Tryggvason, G., Jan, Y.-J., Esmaeeli, A., Unverdi, S.O., 1992. Full simulations of multi-bubble flows. In: Proceedings of Second International Symposium on Propeller and Cavitation. Hangzhou, China, Sept. 1–4.
Tryggvason, G., Ma, M., Lu, J., 2016. DNS assisted modeling of bubbly flows in vertical channels. Nucl. Sci. Eng. 184, 312–320.
Tuković, v., Jasak, H., 2012. A moving mesh finite volume interface tracking method for surface tension dominated interfacial fluid flow. Comput. & Fluids 55, 70–84.
Urbano, A., Tanguy, S., Huber, G., Colin, C., 2018. Direct numerical simulation of nucleate boiling in micro-layer regime. Int. J. Heat Mass Transfer 123, 1128–1137.
Van Der Geld, C.W.M., 2009. The dynamics of a boiling bubble before and after detachment. Heat Mass Transf. 45 (7), 831–846.
Van Helden, W.G.J., Van der Geld, C.W.M., Boot, P.G.M., 1995. Forces on bubbles growing and detaching in flow along a vertical wall. Int. J. Heat Mass Transfer 38 (11), 2075–2088.
VDI, e.V. (Ed.), 2010. VDI Heat Atlas. Springer, Berlin, Heidelberg.
Veldhuis, C.H.J., Biesheuvel, A., van Wijngaarden, L., Lohse, D., 2005. Wake structure of a rising spherical particle. Nonlinearity 18, C1–C8.
Verschoof, R.A., van der Veen, R.C.A., Sun, C., Lohse, D., 2016. Bubble drag reduction requires large bubbles. Phys. Rev. Lett. 117, 104502.
Villermaux, E., Wang, X., Deike, L., 2022. Bubbles spray aerosols: Certitudes and mysteries. PNAS Nexus 1 (5), pgac261.
Van der Waals, J.D., 1979. The thermodynamic theory of capillarity under the hypothesis of a continuous variation of density. J. Stat. Phys. 20 (2), 200–244.
Wang, C.H., Dhir, V.K., 1993. Effect of surface wettability on active nucleation site density during pool boiling of water on a vertical surface. J. Heat Transf. 115, 659–669.
Wang, J., Wang, H., Xiong, J., 2023. Experimental investigation on microlayer behavior and bubble growth based on laser interferometric method. Front. Energy Res. 11, 1130459.
Wang, Y., Zaytsev, M.E., Lajoinie, G., The, H.L., Eijkel, J.C.T., van den Berg, A., Weckhuysen, B.M., Zhang, X., Zandvliet, H.J.W., Lohse, D., 2018. Giant and explosive plasmonic bubbles by delayed nucleation. Proc. Nat. Acad. Soc. 115, 7676–7681.
Warnez, M.T., Johnsen, E., 2015. Numerical modeling of bubble dynamics in viscoelastic media with relaxation. Phys. Fluids 27 (6), 063103.
Warrier, G.R., Dhir, V.K., 2006. Heat transfer and wall heat flux partitioning during subcooled flow nucleate boiling. A review. J. Heat Transf. 128 (12), 1243–1256.
Weber, P., Marschall, H., Bothe, D., 2017. Highly accurate two-phase species transfer based on ALE interface tracking. Int. J. Heat Mass Transfer 104, 759–773.
Weiner, A., 2020. Modeling and Simulation of Convection-Dominated Species Transfer at Rising Bubbles (Ph.D. thesis). Technical University of Darmstadt, Mathematical Modeling and Analysis.
Weiner, A., Bothe, D., 2017. Advanced subgrid-scale modeling for convection-dominated species transport at fluid interfaces with application to mass transfer from rising bubbles. J. Comput. Phys. 347, 261–289.
Weiner, A., Claassen, C., Hierck, I., Kuipers, J., Baltussen, M., 2022. Assessment of a subgrid-scale model for convection-dominated mass transfer for initial transient rise of a bubble. AIChE J. 68 (7), e17641.
Weiner, A., Hillenbrand, D., Marschall, H., Bothe, D., 2019a. Data-driven subgrid-scale modeling for convection-dominated concentration boundary layers. Chem. Eng. Technol. 42 (7), 1349–1356.
Weiner, A., Timmermann, J., Pesci, C., Grewe, J., Hoffmann, M., Schlüter, M., Bothe, D., 2019b. Experimental and numerical investigation of reactive species transport around a small rising bubble. CES: X 1, 100007.
Witharana, S., Phillips, B., Strobel, S., Kim, H.D., McKrell, T., Chang, J.-B., Buongiorno, J., Berggren, K.K., Chen, L., Ding, Y., 2012. Bubble nucleation on nano- to micro-size cavities and posts: An experimental validation of classical theory. J. Appl. Phys. 112, 064904.
Xu, J.-J., Li, Z., Lowengrub, J., Zhao, H., 2006. A level-set method for interfacial flows with surfactant. J. Comput. Phys. 212 (2), 590–616.
Xu, J.-J., Yang, Y., Lowengrub, J., 2012. A level-set continuum method for two-phase flows with insoluble surfactant. J. Comput. Phys. 231 (17), 5897–5909.
Yan, S.R., Shirani, N., Zarringhalam, M., Toghraie, D., Nguyen, Q., Karimipour, A., 2020. Prediction of boiling flow characteristics in rough and smooth microchannels using molecular dynamics simulation: Investigation the effects of boundary wall temperatures. J. Mol. Liq. 306.
Young, N., Goldstein, J., Block, M.J., 1959. The motion of bubbles in a vertical temperature gradient. J. Fluid Mech. 6 (3), 350–356.
Zamansky, R., Le Roy De Bonneville, F., Risso, F., 2024. Turbulence induced by a swarm of rising bubbles from coarse-grained simulations. J. Fluid Mech. 984, A68.
Zanutto, C., Paladino, E., Evrard, F., van Wachem, B., Denner, F., 2022. Modeling of interfacial mass transfer based on a single-field formulation and an algebraic VOF method considering non-isothermal systems and large volume changes. Chem. Eng. Sci. 247, 116855.
Zeng, B., Chong, K.L., Wang, Y., Diddens, C., Li, X., Detert, M., Zandvliet, H.J.W., Lohse, D., 2021. Periodic bouncing of a plasmonic bubble in a binary liquid by competing solutal and thermal marangoni forces. Proc. Natl. Acad. Sci. USA 118 (23), e2103215118.
Zeng, L.Z., Klausner, F., Bernhard, M., Mei, R., 1993. A unified model for the prediction of bubble detachment diameters in boiling systems - II. Flow boiling. Int. J. Heat Mass Transfer 36 (9), 2271–2279.
Zenit, R., Magnaudet, J., 2008. Path instability of rising spheroidal air bubbles: A shape-controlled process. Phys. Fluids 20 (6), 061702.
Zhang, L., Han, J., Wang, H., Car, R., E, W., 2018. Deep potential molecular dynamics: A scalable model with the accuracy of quantum mechanics. Phys. Rev. Lett. 120, 143001.
Zhong, J., Alibakhshi, M.A., Xie, Q., Riordon, J., Xu, Y., Duan, C., Sinton, D., 2020. Exploring anomalous fluid behavior at the nanoscale: Direct visualization and quantification via nanofluidic devices. Acc. Chem. Res. 53, 347–357.
Zhou, P., Hua, S., Gao, C., Sun, D., Huang, R., 2021. A mechanistic model for wall heat flux partitioning based on bubble dynamics during subcooled flow boiling. Int. J. Heat Mass Transfer 174, 121295.
Zipoli, F., Laino, T., Stolz, S., Martin, E., Winkelmann, C., Curioni, A., 2013. Improved coarse-grained model for molecular-dynamics simulations of water nucleation. J. Chem. Phys. 139.
Zupancic, M., Gregori, P., Bucci, M., Wang, C., Matana Aguiar, G., Bucci, M., 2022. The wall heat flux partitioning during the pool boiling of water on thin metallic foils. Appl. Therm. Eng. 200, 117638.